The Astrophysical Journal, 806:263 (18pp), 2015 June 20 doi:10.1088/0004-637X/806/2/263

DOUBLE COMPACT OBJECTS. III. GRAVITATIONAL-WAVE DETECTION RATES

Michal Dominik[1], Emanuele Berti[2], Richard O'Shaughnessy[3], Ilya Mandel[4], Krzysztof Belczynski[1,5], Christopher Fryer[6], Daniel E. Holz[7], Tomasz Bulik[1], and Francesco Pannarale[8]
[1] Astronomical Observatory, University of Warsaw, Al. Ujazdowskie 4, 00-478 Warsaw, Poland
[2] Department of Physics and Astronomy, The University of Mississippi, University, MS 38677, USA
[3] Center for Gravitation, Cosmology, and Astrophysics, University of Wisconsin-Milwaukee, Milwaukee, WI, USA
[4] School of Physics and Astronomy, University of Birmingham, Edgbaston, Birmingham B15 2TT, UK
[5] Center for Gravitational Wave Astronomy, University of Texas at Brownsville, Brownsville, TX 78520, USA
[6] CCS-2, MSD409, Los Alamos National Laboratory, Los Alamos, NM 87545, USA
[7] Enrico Fermi Institute, Department of Physics, and Kavli Institute for Cosmological Physics University of Chicago, Chicago, IL 60637, USA
[8] School of Physics and Astronomy, Cardiff University, The Parade, Cardiff CF24 3AA, UK
Received 2014 May 29; accepted 2015 May 13; published 2015 June 23

ABSTRACT

The unprecedented range of second-generation gravitational-wave (GW) observatories calls for refining the predictions of potential sources and detection rates. The coalescence of double compact objects (DCOs)—i.e., neutron star–neutron star (NS–NS), black hole–neutron star (BH–NS), and black hole–black hole (BH–BH) binary systems—is the most promising source of GWs for these detectors. We compute detection rates of coalescing DCOs in second-generation GW detectors using the latest models for their cosmological evolution, and implementing inspiral-merger-ringdown gravitational waveform models in our signal-to-noise ratio calculations. We find that (1) the inclusion of the merger/ringdown portion of the signal does not significantly affect rates for NS–NS and BH–NS systems, but it boosts rates by a factor of ∼1.5 for BH–BH systems; (2) in almost all of our models BH–BH systems yield by far the largest rates, followed by NS–NS and BH–NS systems, respectively; and (3) a majority of the detectable BH–BH systems were formed in the early universe in low-metallicity environments. We make predictions for the distributions of detected binaries and discuss what the first GW detections will teach us about the astrophysics underlying binary formation and evolution.

Key words: binaries: close – gravitational waves – stars: black holes – stars: neutron

1. INTRODUCTION

Nearly a century has passed since Albert Einstein wrote down the field equations of general relativity. A crucial prediction of his theory is the existence of GWs. Observations of the Hulse–Taylor binary pulsar (Taylor & Weisberg 1989) and the double pulsar J0737-3039 (Lyne et al. 2004) leave little doubt of the existence of GWs, with further evidence provided by the recent claim of a detection of a GW-induced *B*-mode polarization of the cosmic microwave background (BICEP2 Collaboration et al. 2014). However, GWs still elude direct observation. The situation should change in the next few years, when a network of second-generation GW observatories—including Advanced LIGO (Harry 2010, henceforth aLIGO), Advanced Virgo (Virgo Collaboration 2009, henceforth AdV), and KAGRA (Somiya 2012)—will start taking data. The unprecedented sensitivity of these observatories will allow them to observe the inspiral and merger of DCOs out to cosmological distances: for example, aLIGO should observe binary neutron stars out to a luminosity distance of ≃450 Mpc ($z \sim 0.1$), while DCOs containing BHs will be observable to much larger distances (e.g., Abadie et al. 2010). Given the cosmological reach of second-generation GW interferometers, a theoretical investigation of the observable DCO populations which incorporates cosmological evolution and accurate models of the gravitational waveforms is particularly timely. This is the goal of this paper, the third in a series (see Dominik et al. 2012, 2013). Our work builds on the results presented in the second paper (Dominik et al. 2013, henceforth Paper 2), where we presented the cosmological distribution of DCOs for a set of four evolutionary models. These models investigated a range of Hertzsprung gap (HG) common envelope (CE) donors, supernova (SN) explosion engines, and BH natal kicks, showing distinct differences in the properties of the resulting DCO populations. Population models were placed in a cosmological context by adopting the star formation history reported in Strolger et al. (2004) and the galaxy mass distribution of Fontana et al. (2006), both of which are redshift-dependent. We performed all calculations assuming two scenarios for metallicity evolution, meant to bracket the uncertainties associated with the chemical composition of the universe. Binary evolution was performed using the `StarTrack` population synthesis code (Belczynski et al. 2008a).

In this work we complete and extend the analysis of Paper 2. We study the detection rates and the expected physical properties of coalescing DCOs at cosmological distances for second-generation GW observatories. The rates are calculated for different sets of gravitational waveform models and different detector sensitivities, representative of aLIGO, AdV, and KAGRA. Several different groups have presented similar estimates and studies in the past decade (e.g., Lipunov et al. 1997; Bethe & Brown 1998; De Donder & Vanbeveren 1998, 2004a; Bloom et al. 1999; Grishchuk et al. 2001; Nelemans et al. 2001; Dewi & Pols 2003; Voss & Tauris 2003a; Nutzman et al. 2004; Pfahl et al. 2005; Postnov & Yungelson 2006; Marassi et al. 2011; Mennekens & Vanbeveren 2014). However, none have combined cosmological DCO populations with accurate GW models to obtain thorough, detector-specific results. Our astrophysical models for DCO formation are reviewed in Section 2. Gravitational waveform models and signal-to-noise ratio (S/N) estimates are discussed in Section 3. Our procedure to compute event rates is presented in Section 4. Event rates and bulk properties of the

detected populations are presented in Section 5. In Section 6 we present and discuss the study by Mennekens & Vanbeveren (2014), the primary result of which is the lack of detectable black hole–black hole (BH–BH) systems. In Section 7 we discuss the possible astrophysical payoff of the first GW detections and important directions for future work.

2. ASTROPHYSICAL MODELS

2.1. Binary Evolution

We begin with a summary of the four `StarTrack` evolutionary models that form the backbone of this work; a more detailed discussion can be found in Dominik et al. (2012, 2013).

(1) *Standard model*. This is our reference model, representing the state of the art in the formation and evolution of binary systems. We consider only field populations here. Rate estimates performed for dense populations in which dynamical interactions between stars are important (i.e., globular clusters and galactic nuclear clusters) have been presented elsewhere (Gültekin et al. 2004; Grindlay et al. 2006; O'Leary et al. 2006; Ivanova et al. 2008; Sadowski et al. 2008; Miller & Lauburg 2009; Downing et al. 2010). Our Standard model uses the "Nanjing" (Xu & Li 2010) λ coefficient in the CE energy balance prescription of Webbink (1984), where the precise value of λ depends on the evolutionary stage of the donor, its zero-age main sequence (ZAMS) mass, the mass of its envelope, and its radius. In turn, these quantities depend on metallicity, which in our simulations varies within the broad range $10^{-4} \leqslant Z \leqslant 0.03$ (recall that solar metallicity corresponds to $Z_{\odot} = 0.02$). The values of λ for high-mass stars ($M_{\rm ZAMS} > 20\,M_{\odot}$) were obtained through private communication with the authors and are not present in Xu & Li (2010).

The impact of the CE outcome on binary populations depends strongly on the evolutionary stage of the donor, as first discussed in Belczynski et al. (2007). The Standard model does not allow for CE events with HG donors. These stars are not expected to possess a clear core-envelope structure (Ivanova & Taam 2004), thus making it difficult for them to eject their outer layers during the CE phase. In our Standard model all CE events with HG donors lead to a prompt merger before a DCO binary is formed, regardless of the aforementioned energy balance.

The model employs a Maxwellian distribution of natal kicks for NSs with 1D rms velocity $\sigma = 265\,{\rm km\,s^{-1}}$, consistent with NS observations (Hobbs et al. 2005). The same distribution is extended to BHs, where we allow for the possibility that the kicks may be reduced due to fallback of material during the SN that leads to BH formation. The reduction in BH kicks is described via

$$V_{\rm k} = V_{\rm max}\left(1 - f_{\rm fb}\right), \tag{1}$$

where $V_{\rm k}$ is the final magnitude of the natal kick, $V_{\rm max}$ is the velocity drawn from a Maxwellian kick distribution, and $f_{\rm fb}$ is a "fallback factor" that depends on the amount of fallback material, calculated according to the prescription given in Fryer et al. (2012). Our Standard model uses the "Rapid" convection-driven, neutrino-enhanced SN engine (Fryer et al. 2012). The SN explosion is sourced from the Rayleigh–Taylor instability and occurs within the first 0.1–0.2 s after the bounce. When used in the context of binary evolution models, this SN engine successfully reproduces the mass gap (Belczynski et al. 2012b) observed in Galactic X-ray binaries (Bailyn et al. 1998; Özel et al. 2010; but see also Kreidberg et al. 2012).

(2) *Optimistic CE*. In this model we allow HG stars to be CE donors. When the donor initiates the CE phase, the CE outcome is determined via energy balance. The remaining physics is identical to the Standard model.

(3) *Delayed SN*. This model utilizes the "Delayed" SN engine instead of the Rapid one. The former is also a convection driven, neutrino enhanced engine, but is sourced from the standing accretion shock instability, and can produce an explosion as late as 1 s after bounce. The Delayed engine produces a continuous mass spectrum of compact objects, ranging from NSs through light BHs to massive BHs (Belczynski et al. 2012b).

(4) *High BH kicks*. In this model the BHs receive full natal kicks, i.e., we set $f_{\rm fb} = 0$ in Equation (1). Otherwise this model is identical to the Standard model.

2.2. Metallicity Evolution

In this paper we employ two distinct metallicity evolution scenarios: "high-end" and "low-end." These are identical to those in our previous study (Paper 2), and a detailed description can be found therein. Employing such calibrations allows us to explore and bracket uncertainties in the chemical evolution of the universe. In both cases the average metallicity decreases with increasing redshift.

The high-end metallicity profile is calibrated to yield a median value of metallicity equal to $1.5\,Z_{\odot}$ (or 8.9 in the "12 +log(O/H)" formalism) at redshift $z = 0$. This calibration was designed to match the upper 1σ scatter of metallicities according to Yuan et al. (2013, see their Figure 2, top-right panel).

The low-end metallicity profile is based on SDSS observations (Panter et al. 2008), from which we infer that one half of the star forming mass of galaxies at $z \sim 0$ has 20% solar metallicity, while the other half has 150% solar metallicity.

3. WAVEFORM MODELS

3.1. Order-of-magnitude Estimates

For any given GW detector the "horizon distance," $D_{\rm h}$, is defined as the luminosity distance at which an optimally oriented (face-on, overhead) canonical $(1.4 + 1.4)\,M_{\odot}$ neutron star–neutron star (NS–NS) binary would be detected at a fiducial threshold S/N, taken to be 8 in this paper. The expectation value of the S/N, ρ, of a signal with GW amplitude $h(t)$ is given by

$$\rho^2 = 4\int_0^{\infty} \frac{|\tilde{h}(f)|^2}{S_{\rm n}(f)} df, \tag{2}$$

where $\tilde{h}(f)$ is the Fourier transform of the signal and $S_{\rm n}(f)$ is the noise power spectral density (PSD) of the detector (see, e.g., Cutler & Flanagan 1994; Poisson & Will 1995). The square root of the noise PSD is plotted in Figure 1 for several advanced interferometers of interest. For example, the aLIGO horizon distance is $D_{\rm h} \simeq 450$ Mpc.

Although the sensitivity of a GW detector network depends on the details of the search pipeline and the detector data quality, we follow Abadie et al. (2010) in considering a single detector with an S/N threshold $\rho \geqslant 8$ as a proxy for

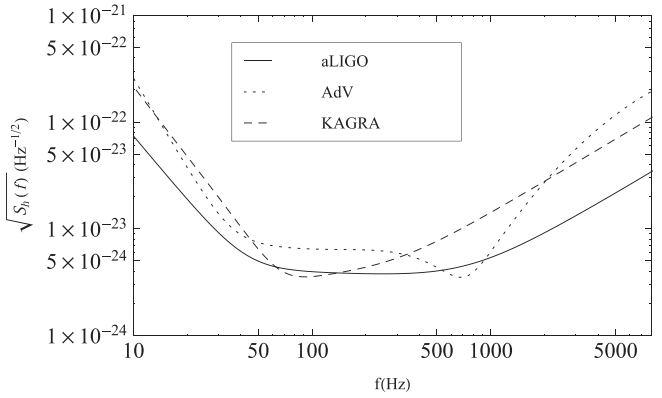

Figure 1. Noise models: we use an analytical approximation to the aLIGO zero-detuning high power (ZDHP) noise power spectral density given in Equation (4.7) of Ajith (2011; we verified that this approximation gives results in excellent agreement with the "official" tabulated aLIGO ZDHP noise PSD given in Shoemaker & LIGO Scientific Collaboration (2010). For AdV we use the fit in Equation (3.4) of Ajith & Bose (2009) to Virgo Collaboration (2009), and for KAGRA we use the PSD fit from the Appendix of Pannarale et al. (2013) to Somiya (2012).

detectability by the network. With this criterion, a simple and common expression to transform the local merger rate to a predicted detection rate $R_{\rm D}$, given the horizon distance $D_{\rm h}$ and the merger rate density, $\mathcal{R}(z)$, evaluated locally (at $z=0$), is

$$R_{\rm D} \simeq \frac{4\pi}{3} D_{\rm h}^3 \left\langle w^3 \right\rangle \left\langle \left(\mathcal{M}_{\rm c}/1.2\,M_\odot\right)^{15/6} \right\rangle \mathcal{R}(0). \qquad (3)$$

In this expression $\langle w^3\rangle^{-1/3} \simeq 2.264$ is a purely geometrical and S/N-threshold-independent factor commonly used to relate sky location- and orientation-averaged distances to optimal detection distances (see the Appendix for details) and $\mathcal{M}_{\rm c} = \eta^{3/5} M$ (where $M = m_1 + m_2$ is the total mass of the binary and $\eta \equiv m_1 m_2 / M^2$) is the "chirp mass" (see, e.g., Cutler & Flanagan 1994). This estimate assumes that (1) cosmological effects are negligible (i.e., space is Euclidean to a good approximation), and (2) most of the S/N is accumulated during an inspiral phase that lasts through the entire sensitive band of the detector, where the GW amplitude in the frequency domain is well approximated by the quadrupole formula, i.e., $\tilde{h}(f) \sim \mathcal{M}_{\rm c}^{5/6} f^{-7/6}/D$. Here D is the luminosity distance to the source. The estimate of Equation (3) follows from this simple scaling together with the definition of the S/N, Equation (2).

Equation (3) involves only the *local* merger rate $\mathcal{R}(0)$ and $\langle \mathcal{M}_{\rm c}^{15/6} \rangle$ is averaged over detected binaries. Both quantities can easily be extracted from `StarTrack` simulations; they are listed in Table 1, along with the values of $R_{\rm D}$ predicted by Equation (3). We expect this rough estimate to be accurate for NS–NS binaries, for which the overwhelming majority of the S/N is accumulated during the inspiral phase. More accurate calculations are required for DCOs comprised of BHs because they are visible out to larger distances (making cosmological corrections important) and because, as we discuss below, a large fraction of the S/N for these binaries comes from the merger/ringdown portion of the signal.

3.2. Including Merger and Ringdown

In order to refine our rate estimates for high-mass systems containing BHs, it is important to consider the full waveform, including inspiral, merger, and ringdown (IMR). The calculation of gravitational waveforms from merging BH–BH and BH–NS binaries requires expensive numerical relativity simulations, but several semi-analytical models have been tuned to reproduce the amplitude and phasing of BH–BH and BH–NS merger simulations. To estimate systematic uncertainties and the impact of spin, we performed rate calculations using three models: (1) the IMRPhenomB model described in Ajith et al. (2011), one of the earliest phenomenological models tuned to both nonspinning and spinning BH–BH simulations with aligned spins, henceforth abbreviated as PhB; (2) the IMRPhenomC (henceforth abbreviated PhC) model by Santamaría et al. (2010), a more accurate alternative to PhB also tuned to nonprecessing simulations of BH–BH mergers; and (3) a nonspinning effective-one-body (EOB) model (Pan et al. 2010). A detailed comparison of the three models can be found in Damour et al. (2011). Recent work by Pannarale et al. (2013) shows that finite-size effects introduce negligible errors ($\lesssim$1%) in S/N calculations for BH–NS binaries; therefore, the above models are adequate for *both* BH–BH and BH–NS binaries. In order to facilitate comparison with previous work, we also evaluated rates using the simplest possible approximation: a restricted post-Newtonian (PN) waveform where the amplitude is truncated at Newtonian order, i.e., $\tilde{h}(f) \sim \mathcal{M}_{\rm c}^{5/6} f^{-7/6}/D$, terminated at a fiducial "innermost stable circular orbit" frequency $f_{\rm ISCO} = (GM\pi/c^3)^{-1} 6^{-3/2}$. At low mass, the upper limit can be neglected and this approximation corresponds to $\rho \propto \mathcal{M}_{\rm c}^{5/6}$, as stated above: see also Equation (7) in O'Shaughnessy et al. (2010a).

Table 1
Local Merger Rates and Simply-scaled Detection Rate Predictions[a]

Model	$\left\langle \mathcal{M}_{\rm c}^{15/6} \right\rangle$ $(M_\odot^{15/6})$	$\mathcal{R}(0)$ (Gpc^{-3} yr^{-1})	$R_{\rm D}$ (aLIGO $\rho \geqslant 8$) (yr^{-1})	$R_{\rm D}$ (3-det network $\rho \geqslant 10$) (yr^{-1})
NS–NS				
Standard	1.1 (1.1)	61 (52)	1.3 (1.1)	3.2 (2.7)
Optimistic CE	1.2 (1.2)	162 (137)	3.9 (3.3)	9.2 (7.7)
Delayed SN	1.4 (1.4)	67 (60)	1.9 (1.7)	4.5 (4.0)
High BH Kicks	1.1 (1.1)	57 (52)	1.2 (1.1)	3.0 (2.7)
BH–NS				
Standard	18 (19)	2.8 (3.0)	1.0 (1.2)	2.4 (2.7)
Optimistic CE	17 (16)	17 (20)	5.7 (6.5)	13.8 (15.4)
Delayed SN	24 (20)	1.0 (2.4)	0.5 (0.9)	1.1 (2.3)
High BH Kicks	19 (13)	0.04 (0.3)	0.01 (0.08)	0.04 (0.2)
BH–BH				
Standard	402 (595)	28 (36)	227 (427)	540 (1017)
Optimistic CE	311 (359)	109 (221)	676 (1585)	1610 (3773)
Delayed SN	829 (814)	14 (24)	232 (394)	552 (938)
High Kick	2159 (3413)	0.5 (0.5)	22 (34)	51 (81)

Note.
[a] Detection rates computed using the basic scaling of Equation (3) for both the *high-end* and *low-end* (the latter in parentheses) metallicity scenarios (see Section 2.2). These rates should be compared with those from more careful calculations presented in Tables 2 and 3.

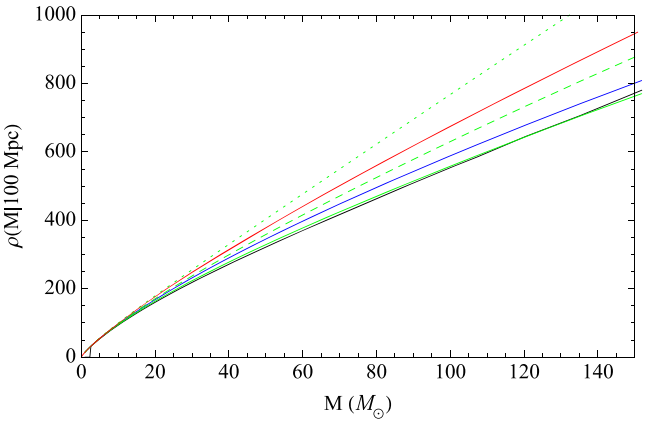

Figure 2. S/N for different signal models: to illustrate the relatively small differences between the signal models we have adopted, we show the S/N, $\rho(M)$, as a function of total binary mass, M, for an equal-mass nonspinning binary at 100 Mpc, where the S/N is evaluated using a single fiducial aLIGO detector. The colored solid curves show (a) the trivial expression $\rho = \rho_0 (M/2.8\,M_\odot)^{5/6}$ with $\rho_0 = 34.3$ (red), (b) an EOB model (black), PhB model (blue), and PhC model (green), all evaluated for zero spin. The green dotted line shows the PhC model evaluated with near-extremal spin on both objects ($\chi_1 = \chi_2 = 0.998$), while the green dashed line shows PhC with near-extremal spin on one object ($\chi_1 = 0.998$, $\chi_2 = 0$). The choice $\chi_i = 0.998$ corresponds to the Thorne (1974) bound. This value of the spin is outside the regime in which phenomenological models have been calibrated, and it has been chosen to provide rough upper limits on the rates.

Figure 2 shows that these models all make similar predictions for the S/N of optimally oriented equal-mass binaries as a function of their total mass for a single aLIGO detector. Even small differences can be important: for any given binary, a 30% difference in amplitude corresponds to a factor $(1.3)^3 \simeq 2.2$ in rate calculations. In practice, however, all nonspinning IMR models agree in S/N to within tens of percent over the total binary mass range of interest (up to 127 $M_\odot$; see Section 5.3). The effect of spin will be discussed in more detail in Section 5.2 below.

Figure 3 shows contour plots of the S/N, ρ, in the (M_z, q) plane, where $M_z \equiv M(1+z)$ is the redshifted total mass, z is the redshift, and $q = m_2/m_1 \leqslant 1$ is the mass ratio of the components, for nonspinning binaries at luminosity distance $D_L = 100$ Mpc. We discuss the justification for considering the S/N as a function of M_z below, but since the chosen distance corresponds to a negligible redshift $z \simeq 0.023$ using the cosmological parameters $\Omega_M = 0.3$, $\Omega_\Lambda = 0.7$, $\Omega_k = 0$, and $h = 0.7$ (chosen for consistency with Dominik et al. 2012, 2013), $M \simeq M_z$ at this distance. The left panel refers to a calculation using an inspiral-only waveform with Newtonian amplitude to compute the horizon distance. The right panel includes inspiral, merger, and ringdown, modeled using the PhC waveform. This plot shows two important features: (1) including the full IMR increases the maximum S/N at this luminosity distance by factors of a few with respect to an inspiral-only calculation, from ≈300 to ≈10^3; (2) high-mass binaries ($M_z \gtrsim 10^{2.5}\,M_\odot \approx 300\,M_\odot$) involving BHs that would not be detectable using inspiral waveforms become detectable using IMR waveforms. The latter point is not important for the field binaries considered in this paper, but it is crucial for intermediate-mass BH mergers (e.g., Amaro-Seoane & Freitag 2006; Fregeau et al. 2006; Belczynski et al. 2014).

In an expanding universe, GW emission is redshifted by the same factor of $(1+z)$ as electromagnetic radiation. In the units ($G = c = 1$) adopted by relativists to describe gravitational waves, the only quantity with dimensions in the GW signal is the total mass M. Since the total mass sets the time scale, a binary source of mass M in the local universe has an identical waveform (but with different amplitude) to a binary at redshift z with mass $M/(1+z)$; see, e.g., Flanagan & Hughes (1998). Equation (2), together with the fact that gravitational amplitudes scale inversely with the luminosity distance $D_L(z)$, implies that the horizon redshift z_h (i.e., the redshift at which an optimally located and oriented binary would have S/N $\rho_{thr} = 8$) can be found via the simple scaling

$$D_h(z_h) = D_L(z)\frac{\rho(M_z, q)}{\rho_{thr}}, \tag{4}$$

where ρ is the S/N at any redshift z, or luminosity distance $D_L(z)$. Note that the right-hand side depends only on z, M_z and q. Therefore one can easily turn an S/N calculation at fixed z (cf. Figure 3) into a plot of the horizon luminosity distance D_h (or equivalently of the horizon redshift z_h) such as Figure 4.

`StarTrack` produces large catalogs of DCOs with intrinsic parameters (M, q), with each of these binaries merging at a different redshift. Any of these representative DCOs is potentially detectable (depending on precise sky location and binary orientation) when $z < z_h$. Determining detectability therefore amounts to a simple interpolation of two-dimensional grids similar to those plotted in Figure 4. These grids can be computed once and for all, given a waveform model and a detector's PSD. Evaluating such a grid typically involves $100 \times 100 = 10^4$ S/N evaluations, and it is much faster than the (impractical) evaluation of millions of S/N integrals such as Equation (2), one for each representative binary produced by `StarTrack`. The conversion between detectability at optimal location and optimal orientation and detectability at generic orientations involves a simple geometrical factor p_{det}, as discussed below.

4. RATE CALCULATION

The detection rate is

$$R_{det} = \iiint_0^\infty \mathcal{R}(z_m)\frac{dt_m}{dt_{det}}p_{det}\frac{dV_c}{dz_m}dz_m dm_1 dm_2, \tag{5}$$

where $\mathcal{R}(z_m) \equiv \dfrac{dN}{dm_1 dm_2 dV_c dt_m}$ is the binary merger rate per unit component mass per unit comoving volume V_c per unit time t_m as measured in the source frame at merger redshift z_m, the term $\dfrac{dt_m}{dt_{det}} = \dfrac{1}{1+z_m}$ accounts for the difference in clock rates at the merger and at the detector, and $p_{det} = p_{det}(z_m; m_1, m_2)$ is the probability (over isotropic sky locations and orientations) that a source with given masses at a given redshift will be detectable. The quantity

$$\frac{dV_c}{dz} = \frac{4\pi c}{H_0}\frac{D_c^2(z)}{E(z)}, \tag{6}$$

with $E(z) = \sqrt{\Omega_M(1+z)^3 + \Omega_k(1+z)^2 + \Omega_\Lambda}$, is the comoving volume per unit redshift, and

$$D_c(z) = \frac{c}{H_0}\int_0^z \frac{dz'}{E(z')} \tag{7}$$

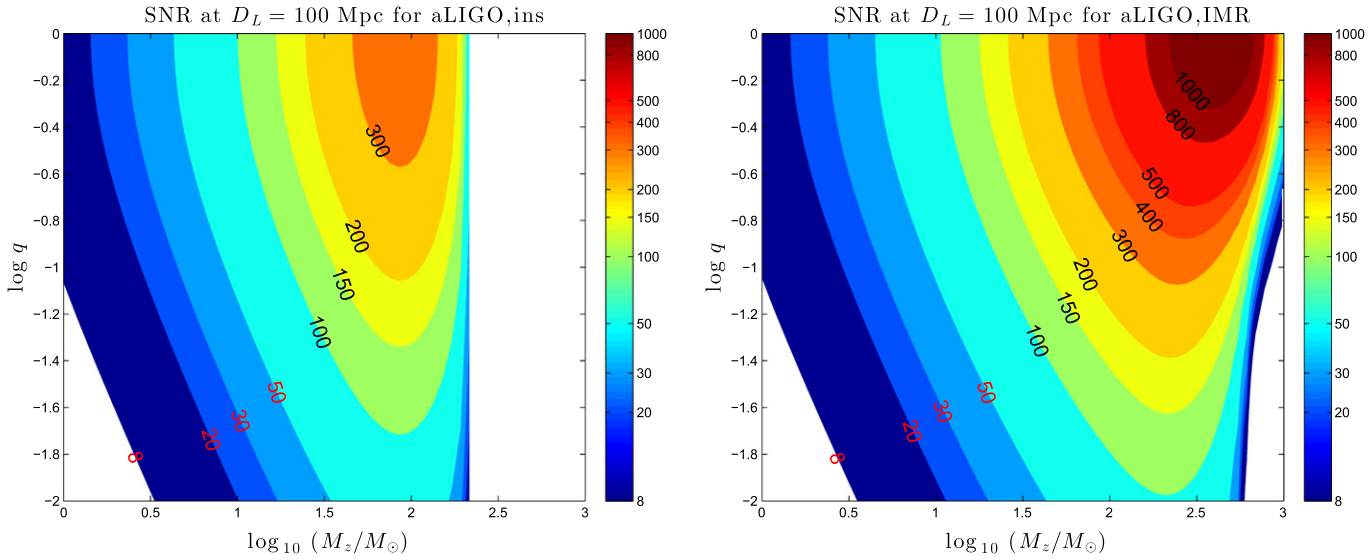

Figure 3. Optimal S/N for nonspinning binaries of given (redshifted) total mass $M_z = M(1+z)$ and mass ratio $q = m_2/m_1$ at luminosity distance $D_L = 100$ Mpc. In the left panel the S/N is computed using the restricted PN approximation (i.e., the GW amplitude is evaluated using the quadrupole formula). In the right panel we use the PhC model for the full IMR waveform; the results for the EOB model are very similar. A low-frequency cutoff of $f_{\rm cut} = 20$ Hz has been assumed (see Section 5.2 for further details).

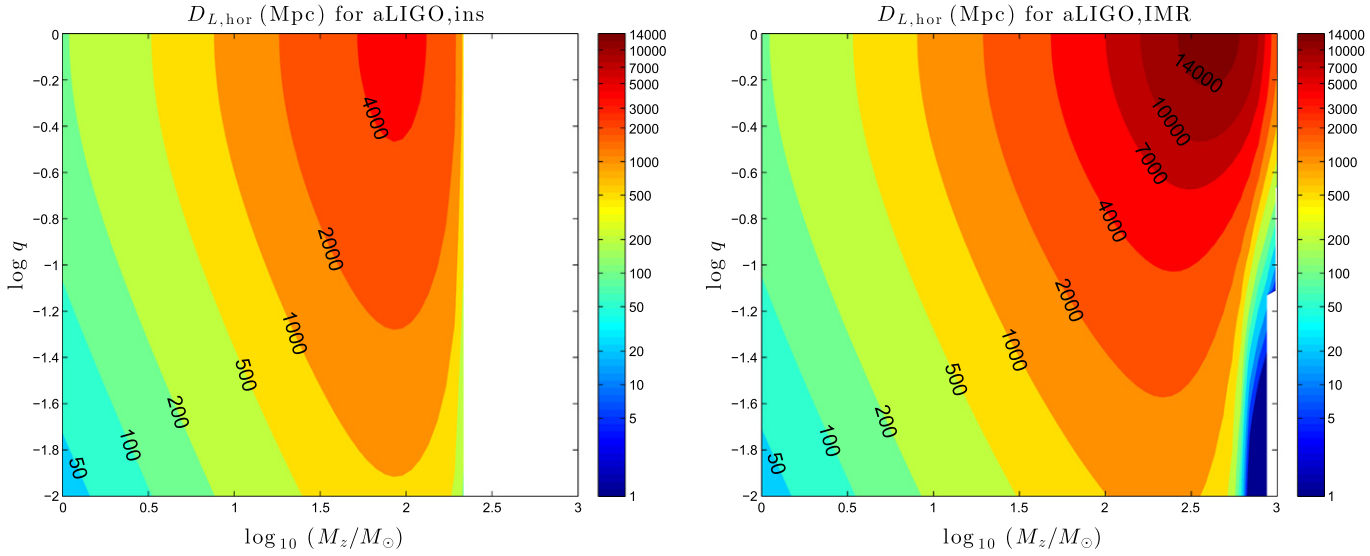

Figure 4. Horizon luminosity distance (in Mpc) for nonspinning binaries as a function of redshifted mass and mass ratio, computed according to Equation (4) using waveforms comprised of only the inspiral (left panel) or the full IMR signal (right panel).

is the comoving distance, related to the luminosity distance $D_{\rm L}(z)$ by $D_{\rm c}(z) = D_{\rm L}(z)/(1+z)$, see Hogg (1999) for our notation and conventions.

The merger rate $\mathcal{R}(z_{\rm m})$ is a convolution of the star formation rate and the number density of binaries per unit star forming mass $M_{\rm f}$ per unit time delay between formation and merger τ:

$$\mathcal{R}(z_{\rm m}) = \int_0^{t_{\rm m}} \int_0^{t_{\rm det}} \frac{dM_{\rm f}}{dV_{\rm c}dt_{\rm f}}(z_{\rm f}) \times \frac{dN}{dM_{\rm f}dm_1dm_2d\tau}(t_{\rm f};\, m_1,\, m_2,\, \tau) \times \delta(t_{\rm m} - t_{\rm f} - \tau)d\tau dt_{\rm f}, \quad (8)$$

where $\mathrm{SFR} = \dfrac{dM_{\rm f}}{dV_{\rm c}dt_{\rm f}}(z_{\rm f})$ is the star formation rate per unit comoving volume per unit time $t_{\rm f}$ at formation redshift $z_{\rm f}$.

The distribution of binaries in mass and time delay space, $\dfrac{dN}{dM_{\rm f}dm_1dm_2d\tau}(t_{\rm f};\, m_1,\, m_2,\, \tau)$, is obtained with the `StarTrack` population synthesis code, taking into account the metallicity distribution at the formation redshift as described in Section 2. Since `StarTrack` simulations produce a set of merging binaries with specific component masses and time delays sampling the desired distribution, the integrals above are easily computed via Monte Carlo over the simulated systems. For computational efficiency the outer integral over the time of formation in Equation (8) is binned over $\Delta t_{\rm f} = 100$ Myr segments, while the integral over the merger redshift $z_{\rm m}$ in Equation (5) is transformed into an integral over merger time via $dz_{\rm m} = \dfrac{dz_{\rm m}}{dt_{\rm m}}dt_{\rm m} = H_0\,(1+z)E(z)dt_{\rm m}$ (Hogg 1999). Thus the detection rate integral can be represented as a Monte Carlo

sum over all simulated binaries:

$$R_{\rm det} = \sum \frac{\rm SFR}{\Delta M_{\rm f}} p_{\rm det} \frac{1}{1+z} \frac{dV_{\rm c}}{dz} \frac{dz}{dt} \Delta t, \quad (9)$$

where $\Delta M_{\rm f}$ is the total star-forming mass that was simulated in the Monte Carlo to represent the time bin Δt, all terms but the first are computed at the merger redshift of the simulated source.

The detection probability for a given source at its merger redshift $p_{\rm det}(z, m_1, m_2)$ is simply the fraction of sources of a given mass located at the given redshift that exceed the detectability threshold in S/N, assuming that sources are uniformly distributed in sky location and orbital orientation. If a single detector with an S/N threshold (e.g., $\rho_{\rm thr} = 8$) is used as a proxy for detectability, the detection probability can be expressed as a cumulative distribution function on the projection parameter w. In the Appendix, w is defined such that $w = 0$ when the detector has no response to the gravitational wave, and $w = 1$ for an optimally located and oriented (face-on and directly overhead) binary. The detection probability is

$$p_{\rm det} = P\left(\rho_{\rm thr}/\rho_{\rm opt}\right), \quad (10)$$

where $P(w)$ is the cumulative distribution function on w over different source locations and orientations, and $\rho_{\rm opt}$ is the S/N for an optimally located and oriented binary at redshift z.

5. RESULTS

In Section 3.1 we obtained a rough estimate of event rates by extrapolating the local rate density via the scaling of Equation (3). This extrapolation is expected to provide a good approximation for low-mass systems (and in particular, NS–NS binaries) because in this case the early inspiral makes up most of the signal observable by advanced GW detectors, the signal extends through the detector band, and the detector range is sufficiently low that cosmological corrections to detectability and the dependence of merger rates on redshift can largely be ignored. The approximation will become increasingly inaccurate for high-mass binaries, such as those comprising one or two BHs. In Sections 3.2 and 4 we went beyond this approximation by implementing three "complete" IMR waveform models (EOB, PhC, PhB), and we described how to combine these models with simulations from the `StarTrack` code in order to obtain more accurate estimates of the event rates (see Equation (9)).

The analytical estimates of Section 3.1 with local merger rates based on the `StarTrack` code are presented in Table 1. The more careful event rate calculations of Section 4 are listed in Table 2 (for the high-end metallicity scenario) and Table 3 (for the low-end metallicity scenario).

In these tables, the "single-detector" columns represent estimated detection rates for a single detector with a $\rho \geqslant 8$ threshold for detectability. This is often used as a proxy for rates in multi-detector networks (Abadie et al. 2010). In the "three-detector" columns we consider two alternate detectability thresholds: minimum *network* S/Ns of either 10 or 12 for a three-detector network composed of three instruments located at the LIGO Hanford, LIGO Livingston, and Virgo sites, all with aLIGO sensitivity. The network S/N threshold of 10 would have yielded false alarm rates of roughly once per decade in 2009–2010 initial LIGO and Virgo data (see Figure 3 in Aasi et al. 2013b). This threshold is optimistic for making confident detections if data quality in advanced detectors is similar to that in the initial detectors and the same searches are used. With this in mind, Aasi et al. (2013b) assumed a network S/N threshold of 12 with an additional threshold constraint on the S/N in the second-loudest instrument; we consider a simple S/N threshold of 12. Detection rates using a network S/N threshold were calculated using the same framework as above, but implementing a network-geometry-dependent $P(w)$ described (and fitted) in the Appendix. In the order-of-magnitude estimates described by Equation (3) and provided in Table 1 we employ $\left\langle w^3 \right\rangle \simeq 0.404$ for the three-detector network ($\rho \geqslant 10$), a factor of ~4.6 larger than the value $\left\langle w^3 \right\rangle \simeq (1/2.26)^3 \approx 0.0866$ used for a one-detector network.

We now discuss these rate predictions, their dependence on gravitational waveform models, and the astrophysical properties of DCO populations observable by advanced GW detectors.

5.1. Broad Features of Rate Estimates

The main conclusion of this work is that BH–BH mergers should yield the highest detection rates in all advanced detectors (aLIGO, AdV, and KAGRA), followed by NS–NS mergers, with BH–NS mergers being the rarest. This finding is independent of our evolutionary models and of the details of the gravitational waveforms (however, see Section 7 for discussion). The only exception is the "Optimistic CE" model, where detection rates for BH–NS mergers dominate over NS–NS mergers (with BH–BH mergers still dominating the detection rates). This model makes the assumption that CE events with HG donors do not always end in a premature merger, allowing more binaries to survive the CE and form merging DCOs, and therefore increasing detection rates. As a result the Optimistic CE model yields very large BH–BH rates, comparable to, though a factor of a few below, existing upper limits on the BH–BH binary mergers from initial LIGO/Virgo observations (see, e.g., Abadie et al. 2012; Belczynski et al. 2012a; Aasi et al. 2013a).

Our quantitative predictions for compact binary merger rates are consistent with our previous papers in this series (Dominik et al. 2012, 2013). In particular, we agree with the main conclusion of those papers: detectable BH–BH binaries can be formed over a broad range of metallicities, with a significant proportion forming in highly subsolar environments (Figure 7). On a model-by-model basis our results are in good agreement with prior work, with factor-of-two or smaller differences due to our inclusion of cosmological effects.

As expected, the simple approximation of Equation (3) gives a good order-of-magnitude estimate of the NS–NS detection rates listed in Tables 2 and 3. However, the approximation fails for BH–BH systems. By comparing the detection rates from Table 1 with inspiral rates from Tables 2 and 3, we see that the local universe approximation of Equation (3) overestimates more careful calculations of detection rates by a factor of ~2 for BH–BH systems. The limited signal bandwidth of high-mass systems, the redshift dependence of binary merger rates, and cosmological corrections make simple scaling relations inaccurate over the large volume in which detectors are sensitive to BH–BH systems. On the other hand, as the merger-ringdown phase of these binaries falls within the sensitive band of second-generation interferometers, it provides a significant

Table 2
Detection Rates for Second-generation Detectors in the *High-end* Metallicity Scenario

Model	AdV [$\rho \geqslant 8$]		KAGRA [$\rho \geqslant 8$]		aLIGO [$\rho \geqslant 8$]			3-det Network [$\rho \geqslant 10(12)$]	
	$f_{\rm cut} = 20$ Hz		$f_{\rm cut} = 10$ Hz		$f_{\rm cut} = 20$ Hz			$f_{\rm cut} = 20$ Hz	
	Insp ($\rm yr^{-1}$)	PhC (EOB) ($\rm yr^{-1}$)	Insp ($\rm yr^{-1}$)	PhC (EOB) ($\rm yr^{-1}$)	Insp ($\rm yr^{-1}$)	PhC (EOB) ($\rm yr^{-1}$)	PhC (spin) ($\rm yr^{-1}$)	Insp ($\rm yr^{-1}$)	PhC ($\rm yr^{-1}$)
NS–NS									
Standard	0.3	0.3	0.8	0.7	1.2	1.1	…	2.5 (1.5)	2.4 (1.4)
Optimistic CE	0.9	0.9	2.1	1.9	3.3	3.1	…	6.9 (4.0)	6.5 (3.8)
Delayed SN	0.4	0.4	1.0	0.9	1.6	1.5	…	3.3 (1.9)	3.1 (1.8)
High BH Kicks	0.3	0.3	0.7	0.7	1.1	1.1	…	2.3 (1.4)	2.2 (1.3)
BH–NS									
Standard	0.2	0.2	0.5	0.4	0.7	0.6	0.8	1.5 (0.9)	1.2 (0.7)
Optimistic CE	1.1	1.0	2.9	2.2	4.4	3.6	4.4	9.2 (5.4)	7.4 (4.3)
Delayed SN	0.09	0.07	0.2	0.2	0.4	0.3	0.5	0.8 (0.5)	0.6 (0.3)
High BH Kicks	0.01	0.007	0.02	0.02	0.04	0.03	0.1	0.09 (0.05)	0.07 (0.04)
BH–BH									
Standard	35	41 (38)	70	93 (86)	117	148 (142)	348	236 (144)	306 (177)
Optimistic CE	126	144 (133)	281	366 (333)	491	618 (585)	1554	1042 (588)	1338 (713)
Delayed SN	27	34 (32)	50	81 (75)	90	129 (124)	320	182 (110)	270 (155)
High Kick	0.6	1.0 (0.9)	0.9	2.5 (2.3)	2.1	3.8 (3.8)	12	4.2 (2.7)	8.2 (4.7)

Note.
[a] Detection rates computed for the high-end metallicity evolution scenario using the inspiral ("Insp") and PhC or EOB IMR models for nonspinning binaries. For aLIGO we also list rough upper limits on the rates computed with the IMR PhC model by assuming that BHs have near-maximal aligned spins ($\chi_1 = \chi_2 = 0.998$ for BH–BH systems; $\chi_1 = 0.998$ and $\chi_2 = 0$ for BH–NS systems). The inspiral is calculated using the restricted PN approximation, which overestimates the amplitude (and therefore the detection rates) for low-mass systems (NS–NS) when compared to the full IMR calculations; see Section 3 for details. The last two columns were computed assuming a minimum *network* S/N of 10 (or 12, in parentheses) for a three-detector network composed of three instruments located at the LIGO Hanford, LIGO Livingston, and Virgo sites, all with aLIGO sensitivity. For each detector, $f_{\rm cut}$ is the assumed low-frequency cutoff in the power spectral density; see Section 5.2.

Table 3
Detection Rates for Second-generation Detectors in the *Low-end* Metallicity Scenario

Model	AdV [$\rho \geqslant 8$]		KAGRA [$\rho \geqslant 8$]		aLIGO [$\rho \geqslant 8$]			3-det Network [$\rho \geqslant 10(12)$]	
	$f_{\rm cut} = 20$ Hz		$f_{\rm cut} = 10$ Hz		$f_{\rm cut} = 20$ Hz			$f_{\rm cut} = 20$ Hz	
	Insp ($\rm yr^{-1}$)	PhC (EOB) ($\rm yr^{-1}$)	Insp ($\rm yr^{-1}$)	PhC (EOB) ($\rm yr^{-1}$)	Insp ($\rm yr^{-1}$)	PhC (EOB) ($\rm yr^{-1}$)	PhC (spin) ($\rm yr^{-1}$)	Insp ($\rm yr^{-1}$)	PhC ($\rm yr^{-1}$)
NS–NS									
Standard	0.3	0.3	0.7	0.6	1.1	1.0	…	2.3 (1.3)	2.2 (1.3)
Optimistic CE	0.8	0.7	1.8	1.7	2.9	2.7	…	6.0 (3.5)	5.6 (3.3)
Delayed SN	0.4	0.4	1.0	0.9	1.5	1.4	…	3.2 (1.8)	2.9 (1.7)
High BH Kicks	0.3	0.3	0.7	0.6	1.0	1.0	…	2.1 (1.3)	2.0 (1.2)
BH–NS									
Standard	0.3	0.2	0.7	0.5	1.1	0.8	1.2	2.3 (1.3)	1.8 (1.0)
Optimistic CE	1.4	1.2	3.6	2.8	5.5	4.4	5.7	12 (6.7)	9.4 (5.4)
Delayed SN	0.2	0.1	0.5	0.4	0.8	0.6	0.9	1.7 (0.9)	1.3 (0.7)
High BH Kicks	0.04	0.03	0.09	0.07	0.1	0.1	0.3	0.6 (0.2)	0.5 (0.2)
BH–BH									
Standard	56	66 (61)	106	153 (140)	183	246 (235)	610	369 (226)	514 (292)
Optimistic CE	287	324 (297)	629	828 (745)	1124	1421 (1339)	3560	2384 (1336)	3087 (1633)
Delayed SN	53	64 (59)	97	152 (139)	171	241 (231)	596	345 (213)	501 (291)
High Kick	0.9	1.5 (1.4)	1.4	3.8 (3.6)	3.2	5.9 (5.8)	19	6.6 (4.0)	13 (7.2)

Note.
[a] Same as Table 2, but for the *low-end* metallicity scenario.

contribution to the S/N. Indeed, as can be seen in Tables 2 and 3, the full IMR calculations increase the detection rates considerably. However, BH–BH detection rates computed with appropriate cosmological corrections are still lower than local merger rates converted into detection rates via the basic scaling of Equation (3).

5.2. Impact of Waveform Models on Predicted Rates

Our results show that the merger–ringdown contribution is not important for estimating detection rates of DCOs containing NSs. In fact, when compared with the restricted PN model, the IMR waveforms slightly *decrease* event rates for NS–NS and BH–NS systems. The reason for this reduction is that IMR waveforms (such as PhC and EOB) provide a more accurate representation of the early inspiral, incorporating PN amplitude corrections that *reduce* the signal amplitude[9]—and hence the event rates—for signals dominated by the early inspiral.

BH–NS systems may be subject to an additional event rate reduction mechanism. There is the possibility of the NS being distorted and disrupted by the BH tidal field. When these violent phenomena occur, a suppression of the GW amplitude takes place before the ISCO frequency, and the S/N decreases with respect to that of a BH–BH system with the same properties. The GW shut-off due to NS tidal disruption depends on the parameters of the system: large values of the mass ratio, the BH spin, the NS radius and the low tilt angles of NS orbital angular momentum relative to BH spin all favor NS disruption (e.g., Belczynski et al. 2008b). By using point-particle IMR waveforms to describe the GW emission of BH–NS systems we are neglecting this event rate reduction mechanism. While it would be possible to take these effects into account for nonspinning systems by using the GW amplitude model of Pannarale et al. (2013), accurate models for systems with spinning BHs do not exist yet. For consistency we therefore use BH–BH waveform models in both cases. Additionally, Pannarale et al. (2013) found that in the nonspinning case, the S/N difference between the mergers of disrupted BH–NS systems and the undisrupted systems modeled with PhC is less than 1%.

Including the merger portion of the signal is important for BH–BH systems. For illustration, let us focus on the Standard model: if we use PhC waveforms rather than the restricted PN approximation, we find a ∼25% increase in the detection rates of BH–BH systems, from 117 (183) to 148 (246) in the *high-end* (*low-end*) metallicity scenario.

The rates predicted by EOB and PhC models agree quite well.[10] This can be understood by looking again at Figure 2, which shows that different approximations of the strong-field merger waveform agree rather well (at least in the equal-mass limit) on the S/N ρ and hence on the predicted event rates, which scale with the cube of the S/N. Waveform differences produce systematic rate uncertainties significantly less than a factor of 2, much smaller than astrophysical differences between our preferred models.

Our detailed calculation shows that typically PhC models overestimate the rates by about 10% when compared to EOB models. This agreement is nontrivial, because the two families of models are very different in spirit and construction: the PhC family is a frequency-domain model that can be easily implemented in rate calculations, while the time-domain EOB model is more accurate in its domain of validity and more computationally demanding. It is important to note that in order to use the two families of models in rate calculations we must compute waveforms and S/Ns in regions of the parameter space where the models were not tuned to numerical relativity simulations. In particular, both models become less accurate for small mass-ratio binaries.

Besides systematic errors in waveform modeling, the detection rates reported in this work (and the resulting distribution of detectable DCO parameters) depend on our detection criteria. We ignore a variety of complications of the detection pipelines, such as the difficulty of searching for precessing sources, noise artifacts (non-stationary, non-Gaussian "glitches" in the instruments) which can make searches for shorter, high-mass signals less sensitive, and the limited uptime of detectors. Instead, we have assumed several simplistic detection thresholds on single-detector or network S/N that are constant across all masses and mass ratios.

Moreover, achieving good detector sensitivity at low frequencies may prove particularly difficult. We have only included bandwidth above specified low-frequency cutoffs ($f_{\rm cut} = 20$ Hz in most cases) for detection-rate calculations. However, the specific choice of low frequency cutoff has minimal impact on our results. For example, using a lower cutoff $f_{\rm cut} = 10$ Hz rather than $f_{\rm cut} = 20$ Hz in the single-detector, high-end metallicity aLIGO rate calculation would increase the Standard model BH–BH rates from 117 to 128 in the inspiral case, and from 148 to 161 in the IMR case. The effect is even smaller for BH–NS and NS–NS rates.

The impact of spins on the predicted detection rates can be important. We only consider BH spins, since NSs in compact binaries are not expected to be rapidly spinning (e.g., Mandel & O'Shaughnessy 2010) and the dynamical impact of NS spin will be small. In Tables 2 and 3 we use the PhC model to estimate the possible impact of BH spin on BH–NS and BH–BH detection rates by assuming that all BHs are nearly maximally spinning (i.e., with dimensionless spin parameter $\chi_1 = \chi_2 = 0.998$) and aligned with the orbital angular momentum. Aligned BH spins cause an orbital hang-up effect that increases the overall power radiated in the merger, produces a rapidly spinning merger remnant, and therefore increases the range to which high-mass binaries can be detected.

We find that spin effects may increase BH–BH detection rates by as much as a factor of 3. These increased rates are a direct result of the increased horizon distance to spinning binaries. For example, a (30+30) $M_\odot$ binary can be observed to roughly 1.3 times farther and be detected $\simeq (1.3)^3 \simeq 2$ more often with near-maximal spins than with zero spin. Additionally, spin dynamics can provide a direct diagnostic of the dominant physical effects in DCO formation (Gerosa et al. 2013). Spin effects only marginally increase BH–NS rates, but (as discussed at the beginning of this section) tidal disruption, which we neglected, may have the opposite effect.

5.3. Astrophysical Properties of Observable DCOs

We now turn to a more detailed analysis of the observable properties of DCOs. For concreteness we will focus on aLIGO results for the "Standard model" and nonspinning PhC waveforms, unless stated otherwise.

NS–NS. By comparing Tables 2 and 3 we see that the detection rates of NS–NS systems are not sensitive to our differing metallicity evolution scenarios. For simplicity, we therefore only discuss our results for the *high-end* metallicity evolution scenario.

[9] Note that in Equation (3.14) of Santamaría et al. (2010) the coefficient of the dominant correction, $\mathcal{A}_2$, listed in their Equation (A5) is negative.

[10] We also carried out calculations using PhB models, which overestimate rates by about 10% with respect to PhC models. We decided not to report these results in the tables, because the PhB model is less accurate than PhC, although it is easier to implement and less computationally expensive.

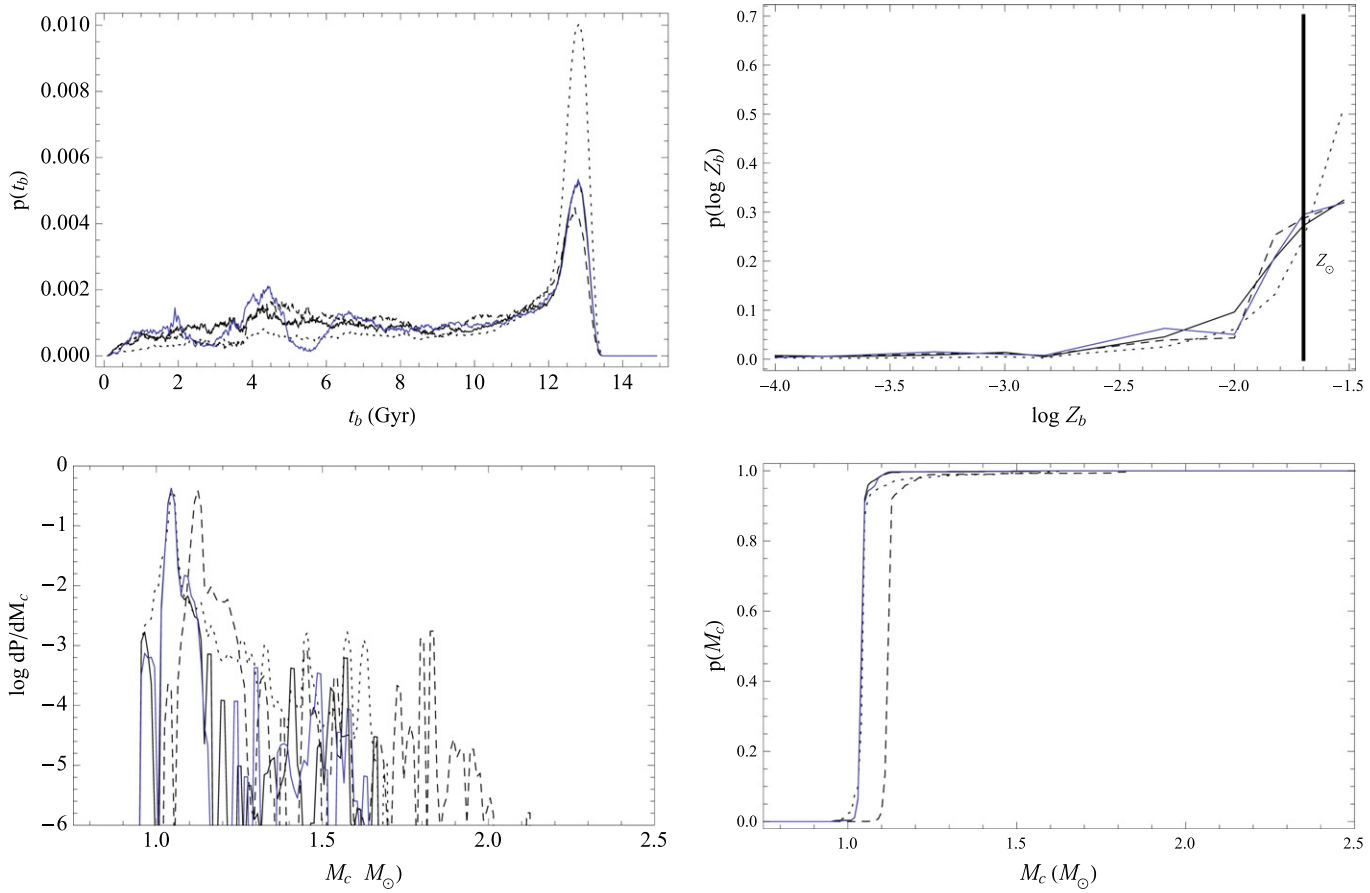

Figure 5. Compact NS–NS binaries detectable by aLIGO: properties of NS–NS binaries with $\rho \geqslant 8$ in a single aLIGO instrument in the high-end metallicity scenario, scaled in proportion to their detection probability. Different color and line styles indicate results for different binary evolution models: Standard model (solid black), optimistic CE (dotted black), delayed SN (dashed black), and high BH kicks (blue). The top left, top right, and bottom left panels show the distribution of birth time t_f, birth metallicity Z_b (with a vertical bar marking solar metallicity, $Z_\odot = 0.02$), and chirp mass $\mathcal{M}_c$, respectively. The bottom right panel shows the cumulative distribution in chirp mass, to highlight significant changes on a linear scale. The time domain ranges from 0 Gyr (Big Bang) to 13.47 Gyr (today). Though our simulations use a discrete array of metallicity bins, to guide the eye their relative contributions have been joined by solid lines in the top right panel; this histogram makes no correction for the density of metallicity bins.

As shown in our previous work (Dominik et al. 2012), NS–NS systems are efficiently created in metal-rich environments. The observable population shares this trait, and half of the observable systems originate from solar metallicities and higher. As the average metallicity content of the universe correlates with time and as most DCOs preferentially merge shortly after formation (i.e., the time delay distribution is $\propto t_{\rm merger}^{-1}$; see Dominik et al. 2012), the birth rate of detectable NS–NS systems peaks at 13 Gyrs after the Big Bang (see Figure 5). The most distant detectable system has a merger redshift $z \sim 0.13$ (or luminosity distance $L_{\rm D} = 610$ Mpc).

The range of possible chirp masses in the bottom left panel of Figure 5 is limited at the low end ($>0.87\,M_\odot$) by the $1\,M_\odot$ minimum birth mass for NS and is limited at the high end by the (assumed) maximum mass for a NS ($m_{\rm NS} < 2.5\,M_\odot$; $\mathcal{M}_{\rm c} < 2.1\,M_\odot$). The birth mass, in turn, is set by SN physics, which we have implemented as the Rapid or Delayed SN engine (Fryer et al. 2012). For this reason the NS mass difference between the SN engines is intrinsic to the entire merging population of NS–NS systems. Therefore, this observable feature should be available to any of the detectors considered in this study.

The chirp mass distributions for Standard and Optimistic CE models span the range from $0.9\,M_\odot$ to $1.6\,M_\odot$. The Delayed SN model results in a notably different NS mass distribution, favoring heavier masses. As the SN explosion in the Delayed engine lasts longer, more matter is accreted onto the proto–NS (which is more massive than in the Rapid engine scenario), allowing the formation of more massive remnants (see Figure 5). The maximum allowed NS mass in this model is $2.5\,M_\odot$, and in extreme (but very rare) cases this mass is approached; the maximum chirp mass for a detectable system in our Monte Carlo simulation was $2.1\,M_\odot$, corresponding to both components close to the maximum allowed limit. For comparison, chirp masses of NS–NS systems in the models utilizing the Rapid SN engine (Standard, Optimistic CE and High BH kick) never exceed $1.7\,M_\odot$. Such extremely high masses are rare for all engines, however, and the majority of chirp masses are much lower, as seen in Figure 5. The presence of more massive systems in the Delayed SN models extends the horizon of NS–NS detectability to $z \sim 0.16$ ($L_{\rm D} = 765$ Mpc).

Last, we note that Standard and High BH kick models are identical for NS–NS systems. The difference between the black curve (Standard) and blue curve (High BH Kick) in Figure 5 corresponds to the systematic errors associated with Monte Carlo errors of binary simulations, galaxy sampling, metallicity binning, etc.

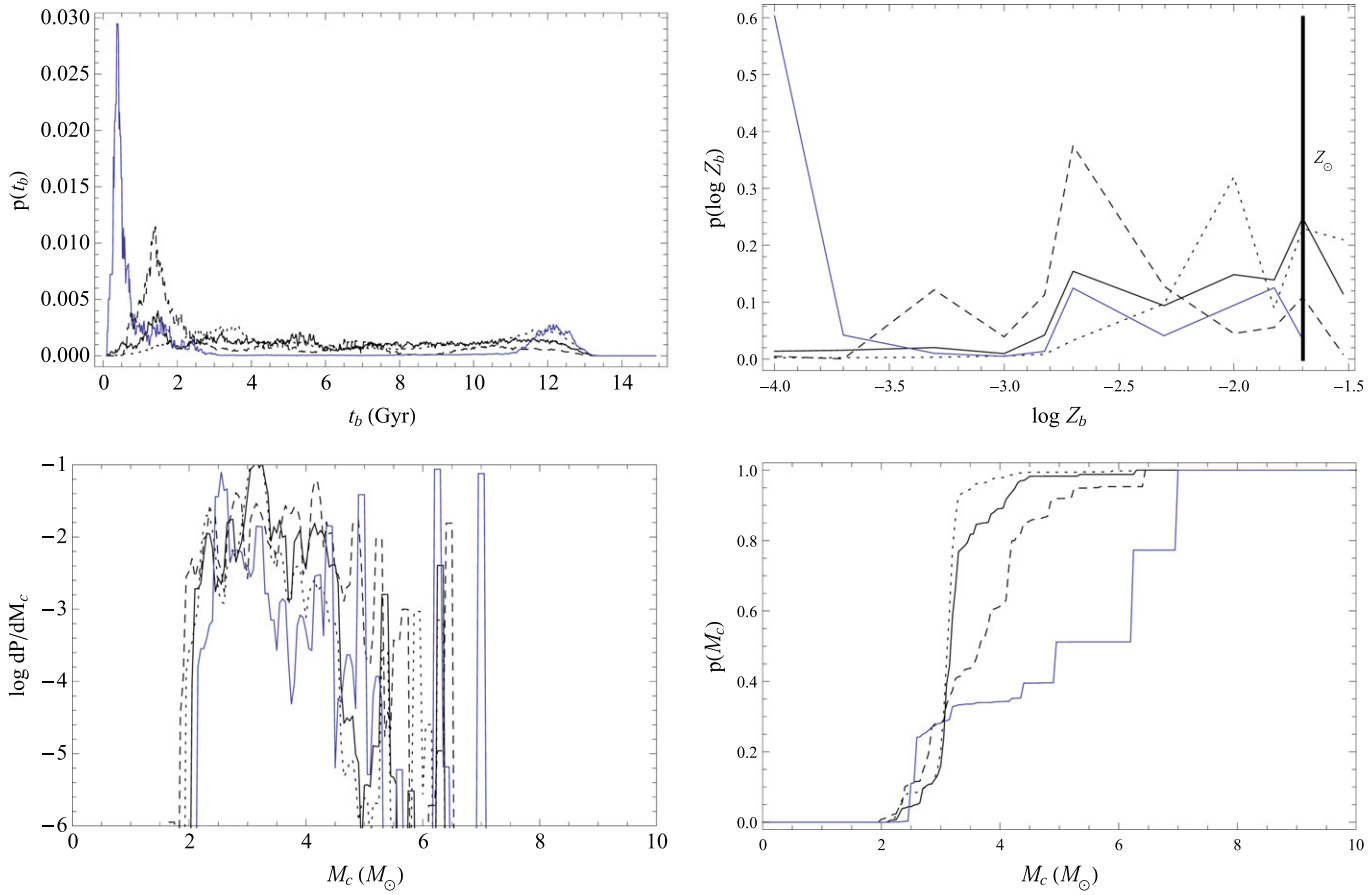

Figure 6. Compact BH–NS binaries detectable by aLIGO: same as Figure 5, but for BH–NS binaries in the high-end metallicity scenario. Some of the sharp features in the chirp mass distribution are an artifact of the crude binning in metallicity undertaken for computational reasons; see the discussion in Section 5.3.

BH–NS. In our previous study (Dominik et al. 2013) we showed that BH–NS systems are efficiently created at moderate metallicities ($Z \sim 0.1\,Z_\odot$, or $\log(Z) \sim -2.7$). Indeed, Figure 6 shows that about half of all detectable BH–NS systems will originate from metallicities $Z < 0.5\,Z_\odot$ ($\log(Z) < -2$). These systems have higher chirp masses than NS–NS systems, on average $3.3\,M_\odot$ versus $1.2\,M_\odot$, and therefore the detectors can sample BH–NS systems from a larger volume. However, BH–NS systems are the rarest of all DCOs per unit (comoving) volume. As a consequence, BH–NS binaries typically yield the lowest detection rates. One exception is the Optimistic CE model, in which the merger rate per unit volume is large enough (while still being lower than for NS–NS systems at all redshifts) that BH–NS detection rates are larger than NS–NS rates because they are observed farther (see Table 1 and Figure 6).

In our Standard model BH–NS systems are detectable up to redshift $z \approx 0.28$ ($L_{\rm D} = 1.4$ Mpc). However, in the Delayed SN model this value reaches $z \approx 0.31$ ($L_{\rm D} = 1.6$ Mpc). As discussed earlier, this is due to the more massive NSs (up to $2.4\,M_\odot$) produced by the Delayed engine.

BH–BH. As discussed in our previous papers in this series (Belczynski et al. 2010; Dominik et al. 2012, 2013), BH–BH systems are formed most efficiently in low-metallicity environments. The detectable population reflects this property: about half of all detectable BH–BH systems were created in environments with metallicities $Z < 0.1\,Z_\odot$ ($\log(Z) < -2.7$). As in prior studies (Voss & Tauris 2003b; Belczynski et al. 2010; Dominik et al. 2012, 2013), our calculations imply that BH–BH systems yield the highest detection rates for ground-based interferometers. This is true even in the "High BH kick" model, where the vast majority of binaries containing a BH are disrupted.

Adjusting the metallicity evolution in the universe from *high-end* to *low-end* we see a factor of ~2 increase in detection rates. In the *low-end* scenario the average metallicity in the universe is lower at all times. Low metallicity environments are much more effective at producing merging BH–BH systems than higher ones, hence the increase in the detection rates.

Half of the detectable objects have chirp masses above $14\,M_\odot$. The most massive of these systems originate from environments with very low metallicity content ($Z \sim 0.01\,Z_\odot$). The birth times of detectable BH–BH systems peak at ~1 Gyr after the Big Bang. Additionally, half of these systems were created within ~2 Gyrs of the Big Bang (see top left panel of Figure 7), when the average abundance of heavy elements was much smaller than today.

As seen in Tables 2 and 3, the detection rates of BH–BH systems vary as we change our assumptions between the four models and two metallicity evolution scenarios. By comparing detection rates, for example, found by aLIGO with PhC waveforms, for the *high-end* metallicity model (works for all model choices), we can distinguish two extreme configurations: (1) the High BH kick model yields the lowest rates of merging BH–BH systems ($3.8\,{\rm yr}^{-1}$). This is a direct consequence of assuming the presence of the maximum natal kick

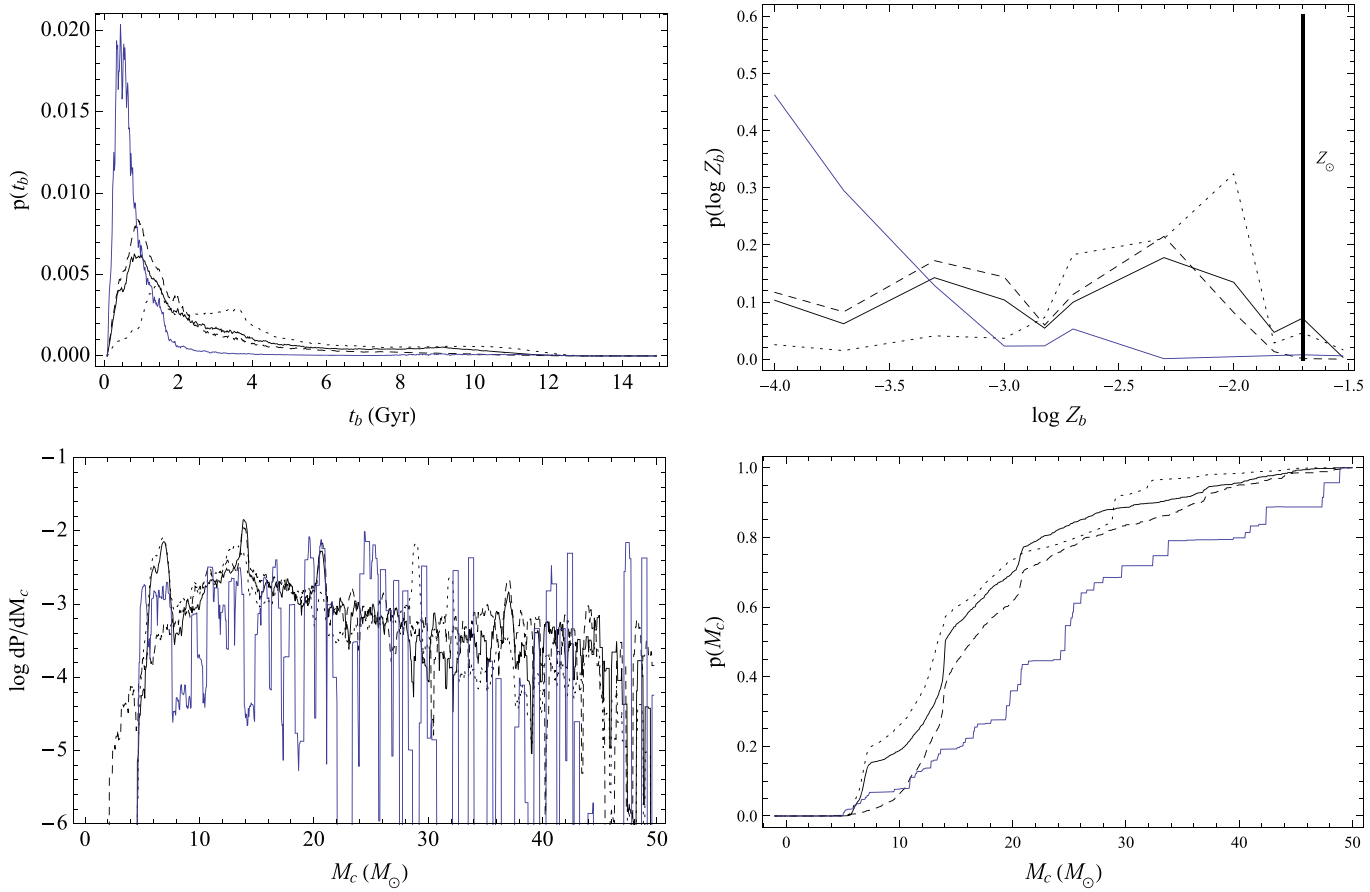

Figure 7. BH–BH binaries detectable by aLIGO: same as Figure 5, but for BH–BH binaries in the high-end metallicity scenario. Some of the sharp features in the chirp mass distribution are an artifact of the crude binning in metallicity undertaken for computational reasons; see the discussion in Section 5.3.

velocities allowed within our framework, which efficiently disrupt BH progenitor binaries. (2) The highest detection rate is achieved with the Optimistic CE model ($618\,\mathrm{yr}^{-1}$). Here, it is assumed that binaries are allowed to progress through the CE with a HG donor, which adds a significant amount of BH–BH systems to the detectable population. The detection rates of the other two models: Standard and Delayed SN are similar to each other (148 and $129\,\mathrm{yr}^{-1}$, respectively).

The farthest objects are detectable out to $z \sim 2$ ($L_\mathrm{D}\,15$ Gpc). These systems consist of the most massive BH pairs ($m_1 = 61\,M_\odot$ and $m_2 = 66\,M_\odot$ in the detectable population, with a chirp mass equal to $55\,M_\odot$), born 1.8 Gyr after the Big Bang, and originating from regions with our lowest considered metallicity content ($Z = 0.005\,Z_\odot$). Note that the maximum mass of BH–BH systems is limited by the maximum ZAMS mass of stars, which was set to $150\,M_\odot$ in the current simulations. The effect of IMF extending to much higher masses on detection of BH–BH inspirals have been recently presented by Belczynski et al. (2014).

The detectable BH–BH chirp mass distribution for the Standard model has three major peaks. These are present at $\sim 7\,M_\odot$, $14\,M_\odot$, and $21\,M_\odot$ (see the black curve in the bottom left and bottom right panels of Figure 7). Their presence is associated with the physics governing the Rapid SN engine and the formation of the most massive BH–BH systems. Within this framework we can distinguish three scenarios for BH formation, each depending on the pre-SN carbon–oxygen (CO) mass (see Equation (16) in Fryer et al. 2012). The "*A*" scenario occurs for $6\,M_\odot < M_\mathrm{CO} \leqslant 7\,M_\odot$ and results in full fallback on the BH and, therefore, no natal kicks (see Equation (1)). The "*B*" scenario occurs for $7\,M_\odot < M_\mathrm{CO} \leqslant 11\,M_\odot$, where the fallback is partial and some natal kicks are present. For this scenario we expect a decreased number of BH–BH systems because of natal kicks disrupting binary systems during SNe. The "*C*" scenario develops for $M_\mathrm{CO} \geqslant 11\,M_\odot$ and again results in full fallback, and no natal kicks.

BH progenitors originating from $Z_\odot$ environments never form through the *C* scenario, since they lose mass in winds at rates that do not allow them to form CO cores larger than $11\,M_\odot$. Since BH–BH progenitors in the *B* scenario are subject to disruption due to the presence of natal kicks, most BH–BH systems in $Z_\odot$ environments form through the *A* scenario, with chirp masses clustered around $7\,M_\odot$.

However, reducing the metallicity by a factor of 2 lowers the wind mass loss rates sufficiently to allow BHs to form through the *C* scenario. At this metallicity ($\sim 0.5\,Z_\odot$) only the most massive progenitors ($M_\mathrm{ZAMS} > 100\,M_\odot$) may form BHs through this scenario. Additionally, the mass of the BHs formed from these high mass components ($M_\mathrm{ZAMS} > 100\,M_\odot$) only depends weakly on their initial mass. This stems from the fact that these stars evolve quickly (~Myrs) and lose large fractions of their hydrogen envelope. Binary evolution does not alter this result significantly, as the interactions between components, such as mass transfer during CE episodes, also lead to the removal of their hydrogen envelopes. The result for

metallicity $\sim 0.5\,Z_{\odot}$ is a clustering of BH–BH systems formed from the most massive binaries at masses around $16\,M_{\odot}$ for each component. This produces the peak in the chirp mass distribution at $\sim 14\,M_{\odot}$.

Reducing the metallicity content by another factor of 2 (to $\sim 0.25\,Z_{\odot}$) allows the same mechanism to form BH–BH systems with masses clustering at around $24\,M_{\odot}$ for each component. These systems form the peak in the chirp mass distribution at $\sim 21\,M_{\odot}$.

The grouping effect disappears when reducing the metallicity abundance in BH progenitors even further. For example, at $0.1\,Z_{\odot}$ the low wind mass loss rate does not increase the separation between components as significantly as for higher metallicities. Consequently, the most massive progenitor binaries engage in a CE phase early in their evolution. This usually happens when the donor is on the HG and the Standard model does not allow for successful outcomes of such CEs. However, this scenario is allowed to form BH–BH systems in the Optimistic CE model, yielding the peak present in the chirp mass distribution at $\sim 29\,M_{\odot}$.

As discussed above, the chirp mass distribution in scenario *C* depends sensitively on the mass loss rate of stars, which depends strongly on metallicity. Binary evolution for $0.5\,Z_{\odot}$ and $0.25\,Z_{\odot}$ creates sharp peaks in the chirp mass distribution of BH–BH systems. In the discrete metallicity grid simulated in this study, there are no metallicity points between $0.5\,Z_{\odot}$ and $0.25\,Z_{\odot}$. Targeted follow-up investigations indicate that metallicity choices between $0.5\,Z_{\odot}$ and $0.25\,Z_{\odot}$ lead to additional sharp peaks in the chirp mass distribution between $14\,M_{\odot}$–$21\,M_{\odot}$. We expect that an integral over a fine grid with appropriately small step sizes in metallicity would lead to all of these narrow peaks merging together to form a single broad distribution without sharp features. However, we cannot confidently describe the shape of this distribution without a more detailed investigation with a fine grid of metallicities, which is not computationally tractable at present.

Finally, the peak in the chirp mass distribution at $\sim 7\,M_{\odot}$ in the Standard model is formed from systems born in 0.5–1 $Z_{\odot}$ environments. These are low-mass BHs (usually 8–9 $M_{\odot}$ per component) formed in the *A* scenario. This formation is particularly interesting as it does not appear in the Delayed SN model, with the difference stemming from the different fallback scenarios in the Rapid and Delayed engines. With the Rapid engine, we can distinguish the three fallback regions. However, the Delayed engine predicts one region of partial fallback for $3.5\,M_{\odot} < M_{\rm CO} \leqslant 11\,M_{\odot}$ and one region of full fallback $M_{\rm CO} \geqslant 11\,M_{\odot}$ (identical to the *C* scenario in the Rapid engine). Since partial fallback implies the presence of natal kicks and, therefore, increased probability of binary disruption, there are no "preferred" masses for the lightest BHs in the Delayed SN engine (see the dashed line in the bottom left panel of Figure 7) as in the Rapid engine.

The Standard and Delayed SN models also yield different lower mass limits for BH remnants (see Section 2). For the "Rapid engine" scenario the lowest-mass BH is $\sim 5\,M_{\odot}$, while for the "Delayed engine" scenario the lowest-mass BH is $\sim 2.5\,M_{\odot}$ (this is also the highest NS mass adopted in our `StarTrack` calculations). As a result, the detectable systems with the lowest total mass have $\mathcal{M}_{\rm c} = 4.8\,M_{\odot}$ and $\mathcal{M}_{\rm c} = 2.4\,M_{\odot}$ in the Rapid and Delayed engine scenarios, respectively.

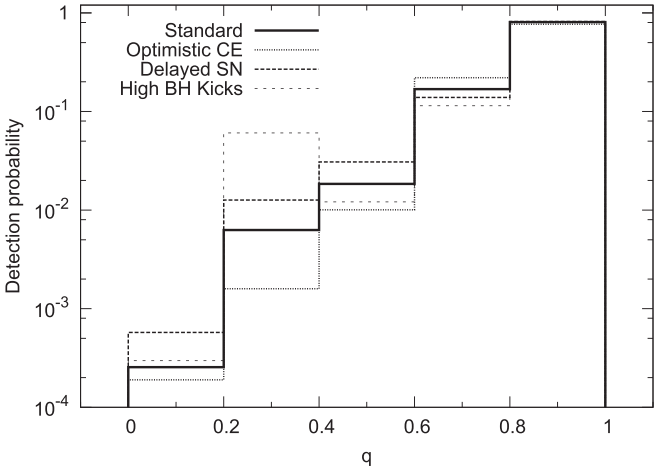

Figure 8. Mass ratio (q) detection probability distribution for BH–BH systems. It is clear that one should expect that the vast majority of detectable BH–BH systems will be formed of nearly equal mass components. The lowest values of q among the detected systems are 0.05 for the Delayed SN model and 0.12 for the remaining models. For each model the probability is normalized to the total number of detections for this model.

Additionally, regardless of our evolutionary models the majority BH–BH systems are formed with nearly equal mass components. Therefore, systems with mass rations ~ 1 dominate the detected population, as shown in Figure 8. For the Delayed SN model the detectable BH–BH systems with the lowest mass ratio have $q \approx 0.05$. For the remaining models this value is $q \approx 0.12$.

For future reference we also present the initial–final mass relation for close BH–BH systems in Figure 9. The relation is divided into the primary (more massive at ZAMS) and secondary (less massive) component for two metallicity values ($Z_{\odot}$ and $0.1\,Z_{\odot}$), for the Standard model. It is clearly visible that binary evolution distorts the initial–final mass relation for single stars in both mass dimensions. In the initial mass dimension, the absence of BHs forming from stars with ZAMS mass above $\sim 70\,M_{\odot}$ is a direct consequence of the assumption of the negative (merger) CE outcome for HG donors in our Standard model. In our framework more massive stars have larger radii and, therefore, are more likely to engage in CE while the donor is on the HG rather than on later evolutionary stages. If this assumption was relaxed (Optimistic CE model) the maximum BH mass reached in close BH–BH systems is found to be $150\,M_{\odot}$ for both metallicities. In the final mass dimension, binary evolution prevents remnant components from reaching masses as high as those formed from single progenitors. Whereas single stars shed mass only through winds, binaries may also remove mass through interactions like the non-conservative mass transfer and/or CE events, which consequently lowers the mass of the remnants.

The initial–final mass relation (in this case for the binary population of close BH–BH systems) is a result of a number of various initial and evolutionary assumptions used in population synthesis calculations. Change of any of these assumptions (whether in initial conditions or evolutionary calculations) may potentially influence the initial–final mass relation and in turn the generated BH–BH population. The largest impact is expected from the treatment of RLOF stability (i.e., criteria for CE development), SN explosion physics, wind mass loss and internal mixing within massive stars induced by convection and/or rotation that sets the radial evolution of massive stars. It

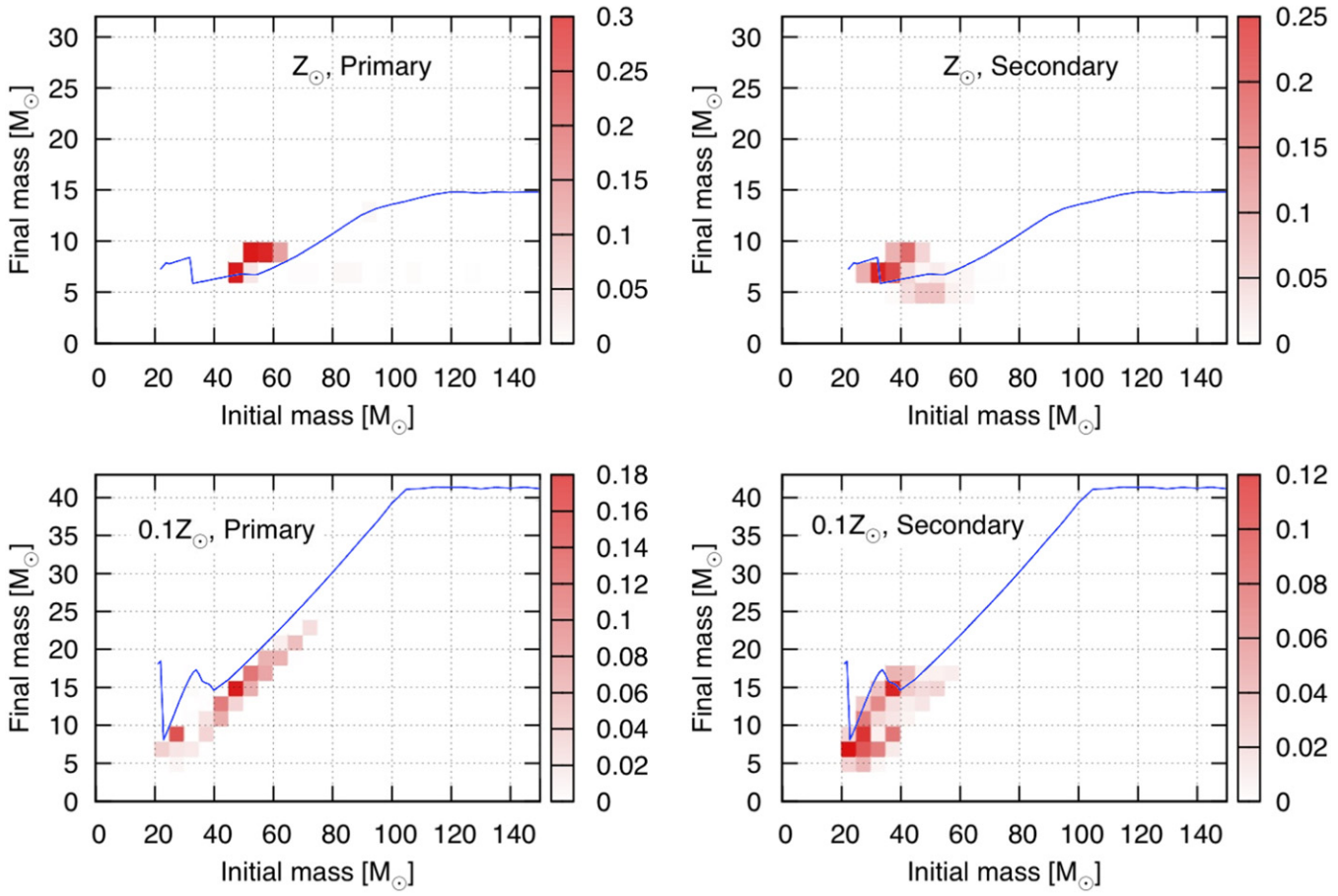

Figure 9. Initial–final mass relation for binary systems. Presented for close BH–BH systems, Standard model. We define primary and secondary components as initially (at ZAMS) more and less massive, respectively. The shaded scale (right side of each panel) shows the fractional contribution of a given ZAMS mass bin to the total mass of merging black holes formed from primaries (left panels) and secondaries (right panels). Note that binary evolution produces a very different initial–final mass relation than the single stellar evolution (thin line). The top panels and bottom panels show results for $Z_{\odot}$ and 0.1 $Z_{\odot}$, respectively.

seems that the change in the assumptions underlying the initial–final mass relation may yield no BH–BHs (Mennekens & Vanbeveren 2014) or numerous BH–BH systems (Voss & Tauris 2003a; Belczynski et al. 2010; Dominik et al. 2012, 2013). However, these results apply only to isolated binary evolution. New studies of globular clusters suggest that, such environments may be the birthplaces of a significant number of BH–BH systems (Rodriguez et al. 2015).

Note that the above relations apply only to BH–BH systems. However, our models do not inhibit the creation of NS from progenitors much more massive than 20 $M_{\odot}$. In fact, the study by Belczynski & Taam (2008) shows that due to binary evolution, NS may form from progenitors as massive as 100 $M_{\odot}$.

6. QUESTIONING THE NO BH–BH THEOREM

During more than a decade of research into the evolution of binary stars and the formation of DCOs, several authors proposed the absence of stellar-mass BH–BH systems merging within the Hubble time (e.g., Nelemans et al. 2001; Mennekens & Vanbeveren 2014). In the latter study the authors have claimed that the main reason for this are the high wind mass loss rates experienced by BH progenitors. For example, in their version of the Brussels population/galactic code (originally De Donder & Vanbeveren 2004b) they fix the wind mass loss rates of the Luminous Blue Variable (LBV) phase at $10^{-3}\,M_{\odot}\,\mathrm{yr}^{-1}$. Following such heavy mass loss, the orbital separation of the components increases so that they do not engage in CE. As the CE is a major mechanism for reducing orbital separation in isolated binary evolution, allowing for the formation of close BH–BH systems, the result is an absence of BH–BH systems detectable through gravitational waves. These results stand in contrast with the works of Voss & Tauris (2003a) and our previous studies (Belczynski et al. 2010; Dominik et al. 2012, 2013).

There are mitigating factors to the finding of Mennekens & Vanbeveren (2014). For example, their code does not allow for tidal interactions between close binary components. As we demonstrate in the following text, tidal interactions may (even for very high LBV winds) allow for the formation of close BH–BH binaries (for more on the importance of tidal interactions, see, e.g., Repetto & Nelemans 2014). Let us consider the following example of binary evolution generated with the StarTrack code. We start with an evolved binary: a 8 $M_{\odot}$ BH accompanied by a 43 $M_{\odot}$ companion at the beginning of the HG phase, with an orbital separation of 4600 $R_{\odot}$ at 5.5 Myr after the creation of the systems (ZAMS). This is a typical phase of a BH–BH progenitor in our Standard model. In this example we also set the LBV wind mass loss rate to $10^{-3}\,M_{\odot}\,\mathrm{yr}^{-1}$ and disable tidal interactions between the components,

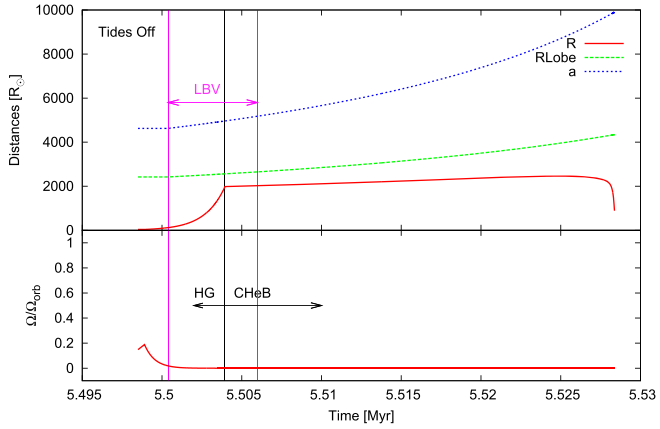

Figure 10. Orbital evolution with tidal interactions disabled. This figure presents a part of the evolution of a 8 $M_\odot$ BH and 43 $M_\odot$ HG system, with the luminous blue variable wind mass loss rate set at $10^{-3}\,M_\odot\,\mathrm{yr}^{-1}$. The top panel shows the evolution of the radius and Roche lobe of the HG star in addition to the orbital separation in the binary. The bottom panel shows the evolution of the HG star's spin frequency relative to the orbital frequency. The HG star's activity as a luminous blue variable is marked by the "LBV" label. The vertical line separating the "HG" and "CHeB" labels marks the transition of the HG star to the core helium burning phase. Note that without tidal interactions the binary's orbit expands (due to stellar wind mass loss) and no component interaction (e.g., CE) is expected. In the end a wide BH–BH binary is formed.

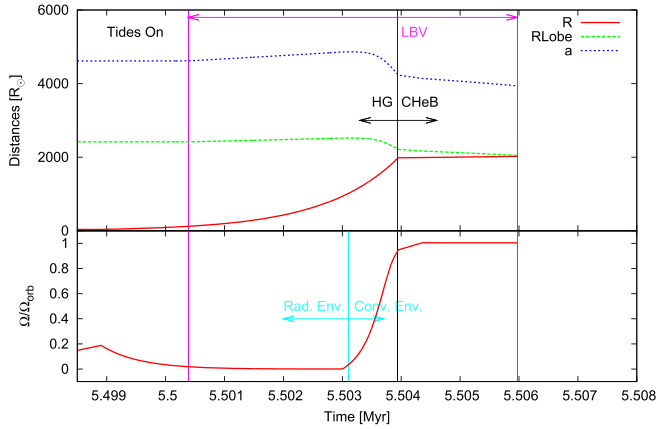

Figure 11. Orbital evolution with tidal interactions enabled. Same as Figure 10 but with tidal interactions enabled. The "Rad. Env." and "Conv. Env." labels along with corresponding arrows highlight areas where the HG star has a radiative and convective envelope, respectively. The vertical line linking the arrows marks the transition point in the structure of the envelope. Tidal interactions allow the transfer of orbital angular momentum into the expanding HG star. The associated orbital decay leads to RLOF and the development of a CE, which allows for the formation of a close BH–BH binary. The timescale on the horizontal axis is zoomed in relative to Figure 10.

both as in Mennekens & Vanbeveren (2014). We find that intense wind mass loss widens the orbital separation between the components to such extent that they never interact. Therefore, when the BH companion forms a second BH, the resulting BH–BH systems is too wide to merge within a Hubble time. This example is presented in Figure 10.

Our exercise can be repeated with tidal interactions between the components enabled. Investigating the same system we find a drastically different outcome of the evolution (see Figure 11). As in the example above, the BH companion starts its significant evolutionary expansion across HG. Due to the conservation of angular momentum, the expansion of the star slows its rotation down almost to a standstill.

Once the companion star fills a sizable fraction of its Roche lobe (∼50%), the tidal torques imposed on the star by an orbiting BH transfer the orbital angular momentum into the star, spinning it up. At first this effect is negligible. However, after approximately 5000 years, when the radius of the star becomes sufficient (∼1100 $R_\odot$), the spin up of the HG star stalls and overpowers the increase of orbital separation. From this point on, the orbital separation starts to decrease for another 3000 years. Finally, when the radius of the star is ∼2000 $R_\odot$, it fills its Roche lobe and initiates a CE.

Our exercise clearly shows that different assumptions may lead to qualitatively different outcomes in terms of the close BH–BH formation. In particular, assumptions used in this study on LBV winds, tidal interactions and radial expansion result in a large number of BH–BH mergers. In contrast, assumptions used by Mennekens & Vanbeveren (2014) result in no BH–BH mergers formed out of the isolated binary evolution.

There are several caveats in this framework. First, it is not theoretically well established if stellar radii can grow to ∼2000 $R_\odot$. For example, intensive mixing (either invoked by rapid rotation or extended convection in the stellar interior) may reduce the size of the H-rich envelope which is responsible for expansion in massive stars. On the other hand the intense wind mass loss may additionally reduce the envelope (e.g., Yusof et al. 2013; but see MESA models for very massive stars; Belczynski et al. 2014). However, the radii of AH Sco, KW Sgr and UY Scuti estimated with the PHOENIX stellar atmosphere model (Wittkowski et al. 2012) extend well beyond 1000 $R_\odot$, with UY Scuti, reaching 1708 $R_\odot$ (Arroyo-Torres et al. 2013). The mass of UY Scuti is estimated to be within 25 $M_\odot$–40 $M_\odot$, i.e., within the mass range for BH progenitors in our framework. Second, the efficiency of tidal interactions depends on the structure of the envelope of the participating components. Stars with convective envelopes tend to respond more strongly to tidal dissipation than stars with radiative envelopes. In `StarTrack` (see Section 3.3 of Belczynski et al. 2008a) we calibrate this phenomenon against the cutoff period for circularization of a population of MS binaries in M67 and the orbital decay accompanying tidal synchronization in the LMC X-4 high mass X-ray binary.

This treatment of tidal dissipation applies directly to the given example as the envelope of the companion star turns from radiative to convective about 3000 years after the companion enters the HG (when HG star radius increases to over ∼1000 $R_\odot$). However, our simulations show that switching tidal dissipation to the weaker radiative damping does not prevent binaries from initiating the CE. In our framework tides are applied to the entire star and we assume that stars rotate non-differentially. It cannot be excluded that tides operate only on the outer layers of stellar atmosphere that holds only a small fraction of a star's mass. Additionally, if there is no (or very weak) transport of angular momentum within a star, only a small fraction of orbital energy is used to synchronize the stellar atmosphere as compared to our prescription. Finally, the moment of inertia of very massive stars depends strongly on the radial profile, and the `StarTrack` assumptions may yield a moment of inertia that is too large, therefore providing a more significant reservoir for depositing orbital angular momentum into the star than is available in practice. If in fact only very little orbital angular momentum is used for binary component synchronization *and* if the winds are in fact as intense as indicated by Mennekens & Vanbeveren (2014), then this

would bar the formation of many close BH–BH binaries found within the framework of our evolutionary model.

Even if tidal interactions turn out to be ineffective in massive close binaries, this does not necessarily rule out the formation of close BH–BH binaries. In field populations about 10%–30% of binaries are, in fact, triples (or higher multiples; e.g., Kiminki & Kobulnicky 2012; Kiminki et al. 2012; Duchêne & Kraus 2013) and Kozai–Lidov effects or dynamical instabilities (Perets & Kratter 2012) may lead to the merger of wide BH–BH binaries. Additionally, many (Kroupa 2014) massive stars are formed in clusters and may be subject to dynamical interactions that can potentially decrease orbital separations. Finally, over the last few years it has been claimed that dense globular clusters may produce significant number of close BH–BH binaries. In contrast with earlier findings with no efficient formation of close BH–BH binaries (e.g., Kulkarni et al. 1993; Sigurdsson & Hernquist 1993; Portegies Zwart & McMillan 2000; Banerjee et al. 2010) the new paradigm emerged based on recent and updated Monte Carlo simulations of dense cluster evolution (e.g., Mackey et al. 2008; Sippel & Hurley 2013; Heggie & Giersz 2014; Morscher et al. 2013). BH–BH binaries may also form via dynamical interactions in galactic nuclear clusters with or without a massive black hole (Miller & Lauburg 2009; O'Leary et al. 2009; but see Tsang 2013).

7. CONCLUSIONS

We have calculated cosmological detection rates of merging DCOs for second-generation GW observatories. We used redshift distributions of merging DCOs from the `Startrack` population synthesis code, and have incorporated the cosmic star formation rate as well as galaxy and metallicity evolution. Using state-of-the-art gravitational waveforms and detector sensitivity curves, we have translated the cosmological merger rates into detection rates for four distinct models of binary evolution.

Our study has several robust implications for imminent GW searches. First and foremost, our four models agree on the detection rates of merging NS–NS systems (∼1 detection per year), with the exception of the Optimistic CE model which predicts rates a factor of 2–3 times higher than other models. The mass distributions of detectable NS–NS systems are also similar across the models, with the exception of the Delayed SN model, which allows for the formation of NSs with higher masses due to prolonged accretion during the SN explosion. We predict that NS–NS binaries will be detectable up to redshift $z \approx 0.13$, i.e., only in the local universe.

Second, BH–NS systems are expected to be the rarest detectable DCOs (less than 1 detection per year), with the exception of the Optimistic CE model, in which BH–NS detection rates slightly exceed those of NS–NS systems of the same model. We predict BH–NS systems to be detectable up to redshift $z \approx 0.3$.

In contrast, BH–BH systems will provide the largest number of detections (∼100–1000 per year), making them the primary target for first detection and the most promising source for future statistical studies of source populations. BH–BH systems dominate event rates even in the pessimistic "High BH kick" model (several events per year), wherein most of the systems containing BHs are disrupted during the SN. Additionally, the BH–BH mass distribution could have rich, observationally accessible structure (various lower limits and shapes) that encodes fine details about stellar and binary evolution (see, e.g., Belczynski et al. 2012b; Fryer et al. 2012; Kreidberg et al. 2012; O'Shaughnessy 2013). We note, however, that the crude binning in metallicity that we had to undertake in order to limit computational costs may create artificial sharp, narrow features in the mass distribution, which would merge together into broader trends with a finer metallicity grid.

Mennekens & Vanbeveren (2014) point out that the detection rate of BH–BH systems may be reduced to zero due to the effects of intense stellar wind during the Red Supergiant and Luminous Blue Variable phases of BH progenitors. However, we have demonstrated that the Mennekens & Vanbeveren (2014) result is a direct consequence of their assumption of no tidal interaction in close binaries. If tides can efficiently transfer angular momentum from the orbit into the companion spin, then it is expected that isolated binaries will form close BH–BH systems.

The criteria for the development of the CE phase may influence the merger and detection rates of all DCOs. Woods & Ivanova (2011) and Ivanova (2015) state that the criterion for the stability of mass transfer sourced from the polytropic approximation is much too strict. Therefore, the frequency of the CE may be overestimated. The CE is a major mechanism for creating close binaries that coalesce within a Hubble time. The lack of CE events would, therefore, decrease the number of DCO mergers. This would provide a reasonable pessimistic scenario for the lack of detections of gravitational wave signals. A study of CE development criteria and its effect on the formation of close BH–BH binaries is underway (K. Belczynski et al. 2015, in preparation). However, an assumed rarity of CE systems would be difficult to reconcile with observational evidence pointing to systems (for example, V1309 Sco, V4332 Sgr, OGLE 2002-BLG-360 or CK Vul) which seem to have developed a CE (e.g., Martini et al. 1999; Tylenda et al. 2011, 2013). Additionally, massive X-ray binaries such as NGC300 X-1 or IC10 X-1 are on close orbits with orbital periods ∼30 hr, which have likely developed through a CE event.

Our study shows that detectable NS–NS systems are formed significantly later in the history of the universe than BH–BH and BH–NS systems. As shown in Figures 5–7, the birth times of NS–NS systems cluster around 13 Gyr after the Big Bang, while for the other systems this is 1 Gyr. This behavior might be counter-intuitive, as the intrinsic distribution of time delays between formation and merger for all types of DCOs falls off as $t_{\rm merger}^{-1}$, barring exceptional circumstances (e.g., near-solar metallicity BH–BH binaries; Dominik et al. 2012). Therefore, one might expect the majority of detectable DCOs to be formed within the past ∼Gyr as is the case for NS–NS systems. However, BH–BH systems are created most efficiently in the lowest metallicity environments, and therefore their formation rate is highest in the early universe. The long time-delay tail of these early systems dominates the subsequent detection rate. The metallicity evolution is therefore a crucial factor in predicting the detectable rate of DCOs.

We also find that including the merger and ringdown components of the GW signal does not have a significant impact on the detection rates of NS–NS systems. The full IMR calculations become important for higher mass systems, and especially for BH–BH binaries. The detection rates for BH–BH systems increases by at least 20%, and typically by ∼50%, when using full IMR waveforms when compared to the PN inspiral alone.

The detection rate of BH–BH systems is also sensitive to spin effects. Extreme aligned spins increase the rates by a factor of ∼3 when compared with the non-spinning case.

We used simplified criteria for detectability, considering an S/N threshold of 8 in a single detector as a proxy for the network (see Abadie et al. 2010). For reference, we also considered a network S/N threshold of 10, which is likely to be very optimistic, and 12, which is more realistic (cf. Aasi et al. 2013b), on a network of three detectors with aLIGO sensitivity. The network S/N threshold of 12 yields rates which are roughly comparable with rates computed using an S/N threshold of 8 in a single aLIGO detector as proxy for the network. The actual detection thresholds are a complicated function of network configuration, the level and frequency of non-Gaussian, non-stationary excursions in the noise, and search pipeline sensitivity to different source types. Therefore, our simple thresholds are only meant to yield rough estimates of detection rates, and the focus should be on relative rates for different source types and model assumptions rather than absolute numbers. Finally, we note that the sensitivity of advanced detectors will gradually improve during commissioning, and several years will pass before they reach the sensitivity we have assumed above (for an approximate time line, see Aasi et al. 2013b).

The detection rates computed by assuming an S/N threshold of 8 in a single aLIGO detector as proxy for the network allow for a direct comparison with the rate ranges compiled in (Abadie et al. 2010), which used the same detectability criterion. Abadie et al. (2010) incorporated a number of population synthesis studies and Galactic binary pulsar observations, but did not include some of the factors considered in the present study, such as cosmology and variations in metallicity distributions and star formation rates with redshift. We find that our predicted detection rates for NS–NS and BH–BH binaries fall within the ranges given in Abadie et al. (2010) for all models and both metallicity distribution choices considered in the present work. For BH–NS binaries, the same holds for all models and metallicity choices except for the high BH kick model, which yields BH–NS detection rates below the range quoted in Abadie et al. (2010).

We note that uncertainties in waveform systematics and detection criteria pale in comparison to uncertainties in stellar and binary evolution. We consider the most important uncertainties to be the progress and outcome of the CE phase, the SN explosion mechanism and the magnitude of BH natal kicks. The four binary evolution models discussed in this study explore these uncertainties, resulting in a wide range of mass distributions and event rates. Changing other parameters such as the initial binary mass distribution or varying the mass escaping the systems during mass transfer episodes would also influence the resulting distributions and rates (O'Shaughnessy et al. 2005, 2008, 2010a).

The properties of the DCO populations produced in our various models are sufficiently differentiated that it may be possible to constrain or rule out some of the input physics based on observed populations. For example, a lack of significant number of detections will disfavor the Optimistic CE model, in which we allow for CE events with HG donors and thus find very high detection rates. This will indicate how (if at all) CE develops for HG stars. If BH–BH systems are not detected far more frequently than other DCO types, a likely explanation is that BHs receive significant natal kicks disrupting their binaries. A detailed comparison of detection rates with current LIGO upper limits can be found in Belczynski et al. (2012a). As detections accumulate, a well measured chirp mass distribution could allow us to distinguish between the Rapid and Delayed SN engine models, which generate continuous and gapped chirp mass distribution of DCOs, respectively. The number of detections needed to distinguish between the Rapid and Delayed SN engines will be discussed in future work (M. Dominik et al. 2014, in preparation).

We thank a number of LIGO and Virgo collaboration colleagues, particularly Thomas Dent, David Shoemaker, Stephen Fairhurst and Peter Saulson, for advice on the manuscript. We thank the N. Copernicus Astronomical Centre in Warsaw, Poland, and the University of Texas at Brownsville, for providing computational resources. The authors acknowledge the Texas Advanced Computing Center (TACC) at The University of Texas at Austin for providing computational resources. K.B. acknowledges support from a Polish Science Foundation Master 2013 Subsidy, Polish NCN grant SONATA BIS 2, NASA grant NNX09AV06A and NSF grant HRD 1242090 awarded to the Center for Gravitational Wave Astronomy at U.T. Brownsville. M.D. acknowledges support from the National Science Center grant DEC-2011/01/N/ST9/00383. E.B. acknowledges support from National Science Foundation CAREER Grant PHY-1055103. R.O.S. was supported by NSF award PHY-0970074 and the UWM Research Growth Initiative. D.E.H. acknowledges support from National Science Foundation CAREER grant PHY-1151836. He was also supported in part by the Kavli Institute for Cosmological Physics at the University of Chicago through NSF grant PHY-1125897 and an endowment from the Kavli Foundation and its founder Fred Kavli. T.B. was supported by the DPN/N176/VIRGO/2009 grant and the DEC-2013/01/ASPERA/ST9/00001 from the National Science Center, Poland. F.P. was supported by STFC grant No. ST/L000342/1. This work was supported in part by the National Science Foundation under grant No. PHYS-1066293 and the hospitality of the Aspen Center for Physics (KB). The study was also sponsored by the National Science Center grant Sonata Bis 2 (DEC-2012/07/E/ST9/01360).

APPENDIX
SINGLE- AND MULTI-DETECTOR RESPONSE

The "expected detection rate for GW detectors" is a theorist's idealization. First and foremost, the event rate depends sensitively on the (time-dependent) performance of instruments in development. Furthermore, real GW searches employ complicated detection thresholds, accounting for noise non-Gaussianity and non-stationarity; for multiple instruments with unequal power spectra; and for some search-dependent consistency requirement across multiple detectors. Rather than attempt realism, our idealizations provide a concrete, reproducible filter to identify the number and (critically) distribution of "detectable" binaries.

A.1. Cumulative Amplitude Distribution for a Single Detector

In a simple idealization, the detection threshold depends only on a single detector's S/N. Several authors have characterized the response of a single GW detector to the angular distribution

of power for a GW source dominated by $(l, |m|) = (2, 2)$ multipole radiation (Finn & Chernoff 1993; Finn 1996; O'Shaughnessy et al. 2010a). This response depends on the two-dimensional sky location Ω, inclination ι, and polarization ψ, and can be conveniently summarized by a projection parameter w which is maximum $(w = 1)$ for a face-on, overhead source, and minimum $(w = 0)$ for sky locations and orientations where the detector has no response to the source. The S/N, $\rho(\Omega, \psi, \iota)$, is equal to the maximum S/N of a face-on, overhead source at the same distance scaled by w, i.e., $\rho = w\rho_{\rm opt}$. The cumulative distribution function for w is $P(w)$:

$$P(w) = \int_V \frac{d\Omega}{4\pi}\frac{d\psi}{\pi}\frac{d\cos\iota}{2}, \tag{11}$$

where we integrate over the four-dimensional angular integration volume, V, which is the set of all Ω, ι, ψ such that the response exceeds w. Our expression is identical to the cumulative distribution function $P(\Theta)$ defined by Finn & Chernoff (1993) and discussed also by Finn (1996), but we use the variable $w = \Theta/4$ such that $0 < w < 1$ (see, e.g., O'Shaughnessy et al. 2010a; Belczynski et al. 2014). Note that $\langle w^2\rangle = (2/5)^2$, therefore the optimal S/N at a given distance and the square root of the angle-averaged signal power for a source at that distance $(\rho^2_{\rm ave} \equiv \langle\rho^2\rangle)$ are related by $\rho_{\rm opt} = (5/2)\rho_{\rm ave}$. Meanwhile, $\langle w^3\rangle^{-1/3} \simeq 2.264$ is the factor commonly used to relate volume-averaged distances to optimal detection distances, where $\langle w^3\rangle$ is the fraction of detectable sources within a sphere whose radius equals the at-threshold detection distance for an optimally located and oriented source; see, e.g., Equation (6) of O'Shaughnessy et al. (2010a).

Easily-interpolated tabulated results for $P(w)$ are available online.[11] The analytic approximation to this distribution function given by Finn (1996) is inadequate for our purposes; our tabulated results follow from sampling the distribution numerically via a Monte Carlo over 10^9 binaries. We found that a good three-parameter fit to the data is

$$\begin{aligned} P(w) = {} & a_2^{(n)}\left[\left(1 - w/\alpha^{(n)}\right)^2\right] \\ & + a_4^{(n)}\left[\left(1 - w/\alpha^{(n)}\right)^4\right] \\ & + a_8^{(n)}\left[\left(1 - w/\alpha^{(n)}\right)^8\right] \\ & + \left(1 - a_2^{(n)} - a_4^{(n)} - a_8^{(n)}\right)\left[\left(1 - w/\alpha^{(n)}\right)^{10}\right], \end{aligned} \tag{12}$$

where (n) refers to the number of detectors in the network, $\alpha^{(n)}$ is the maximum value that w can attain, so that $\alpha^{(1)} = 1$ as w is bounded between 0 and 1, and the coefficients are $a_2^{(1)} = 0.374222$, $a_4^{(1)} = 2.04216$, and $a_8^{(1)} = -2.63948$. Note that Equation (12) ensures that $P(\alpha^{(1)}) = 0$ and $P(0) = 1$.

A.2. Cumulative Amplitude Distribution for Multiple Detectors

For a multi-detector network A, a network S/N ρ_A can always be defined. Following an identical procedure as above, we can define a cumulative distribution P_A that generalizes Equation (11). As before, $w = \rho/\rho_{\rm opt}$, but for multi-detector networks composed of instruments with equal sensitivity, ρ is the network S/N while $\rho_{\rm opt}$ is the single-detector S/N from an optimally oriented binary directly overhead that detector. For three identical instruments at the LIGO Hanford, Livingston, and Virgo sites, tabulated results for P_A are available online at the URL listed in the previous footnote; a good fit to the data has the form given in Equation (12), but now $0 < w < 1.4$, so that $\alpha^{(3)} = 1.4$. The coefficients we obtain are $a_2^{(3)} = 1.19549$, $a_4^{(3)} = 1.61758$, and $a_8^{(3)} = -4.87024$.

Schutz (2011) described a simple idealized model for the sensitivity of multi-instrument networks. This model is almost equivalent to our own. The two models differ in that Schutz (2011), in his Equations (14)–(15), replaces w^2 by an (unphysical) average of w^2 over polarization, then treats the rms value of w (i.e., $\langle w^2\rangle^{1/2}$) as a substitute for w whenever w appears. Our results adopt no such simplifying approximation.

A.3. Higher Harmonics

Real GW sources produce multimodal radiation, with each mode providing a distinct angular pattern. For low-mass sources these higher harmonics contribute little to the detector's response. For high-mass binaries with asymmetric mass ratios, higher harmonics can contribute significantly to the observationally accessible signal (Capano et al. 2014). For nonspinning binaries of total mass $M < 60\,M_\odot$, and with the smaller mass $>1.2\,M_\odot$, we expect higher harmonics to increase the S/N ρ by less than a few percent, consistent with extrapolations derived using PN waveforms. This expectation is supported by investigations carried out with a multimodal EOB IMR waveform (Pan et al. 2011). To a good approximation, the S/N ρ and angular distribution $P(w)$ can be approximated by the corresponding expressions derived assuming purely quadrupolar, (2, 2)-mode emission.

Higher harmonics can play a significant role if the mass distribution extends to very high *redshifted* mass. At high mass, higher harmonics contribute a greater fraction of the S/N, each in a distinctive angular pattern; see O'Shaughnessy et al. (2010b) for illustrative results. For aLIGO, systematic astrophysical uncertainties such as the BH spin and mass have a significantly greater impact than the harmonic content. These higher harmonics will be important for third-generation interferometers, like the Einstein Telescope. This will be investigated in future work.

[11] Data files can be found online at the following URL: http://www.phy.olemiss.edu/~berti/research.html.

REFERENCES

Aasi, J., Abadie, J., Abbott, B. P., et al. 2013a, PhRvD, 87, 022002
Aasi, J., Abadie, J., Abbott, B. P., et al. 2013b, arXiv:1304.0670
Abadie, J., Abbott, B. P., Abbott, R., et al. 2010, CQGra, 27, 173001
Abadie, J., Abbott, B. P., Abbott, R., et al. 2012, PhRvD, 85, 082002
Ajith, P. 2011, PhRvD, 84, 084037
Ajith, P., & Bose, S. 2009, PhRvD, 79, 084032
Ajith, P., Hannam, M., Husa, S., et al. 2011, PhRvL, 106, 241101
Amaro-Seoane, P., & Freitag, M. 2006, ApJL, 653, L53
Arroyo-Torres, B., Wittkowski, M., Marcaide, J. M., & Hauschildt, P. H. 2013, A&A, 554, A76
Bailyn, C. D., Jain, R. K., Coppi, P., & Orosz, J. A. 1998, ApJ, 499, 367
Banerjee, S., Baumgardt, H., & Kroupa, P. 2010, MNRAS, 402, 371
Belczynski, K., Buonanno, A., Cantiello, M., et al. 2014, ApJ, 789, 120
Belczynski, K., Dominik, M., Bulik, T., et al. 2010, ApJL, 715, L138
Belczynski, K., Dominik, M., Repetto, S., Holz, D. E., & Fryer, C. L. 2012a, ApJ, submitted (arXiv:1208.0358)
Belczynski, K., Kalogera, V., Rasio, F. A., et al. 2008a, ApJS, 174, 223

Belczynski, K., & Taam, R. E. 2008, ApJ, 685, 400
Belczynski, K., Taam, R. E., Kalogera, V., Rasio, F. A., & Bulik, T. 2007, ApJ, 662, 504
Belczynski, K., Taam, R. E., Rantsiou, E., & van der Sluys, M. 2008b, ApJ, 682, 474
Belczynski, K., Wiktorowicz, G., Fryer, C. L., Holz, D. E., & Kalogera, V. 2012b, ApJ, 757, 91
Bethe, H. A., & Brown, G. E. 1998, ApJ, 506, 780
BICEP2 Collaboration, Ade, P. A. R., Aikin, R. W., et al. 2014, PhRvL, 112, 241101
Bloom, J. S., Sigurdsson, S., & Pols, O. R. 1999, MNRAS, 305, 763
Capano, C., Pan, Y., & Buonanno, A. 2014, PhRvD, 89, 102003
Cutler, C., & Flanagan, É E. 1994, PhRvD, 49, 2658
Damour, T., Nagar, A., & Trias, M. 2011, PhRvD, 83, 024006
De Donder, E., & Vanbeveren, D. 1998, A&A, 333, 557
De Donder, E., & Vanbeveren, D. 2004a, NewAR, 48, 861
De Donder, E., & Vanbeveren, D. 2004b, NewAR, 48, 861
Dewi, J. D. M., & Pols, O. R. 2003, MNRAS, 344, 629
Dominik, M., Belczynski, K., Fryer, C., et al. 2012, ApJ, 759, 52
Dominik, M., Belczynski, K., Fryer, C., et al. 2013, ApJ, 779, 72
Downing, J. M. B., Benacquista, M. J., Giersz, M., & Spurzem, R. 2010, MNRAS, 407, 1946
Duchêne, G., & Kraus, A. 2013, ARA&A, 51, 269
Finn, L. S. 1996, PhRvD, 53, 2878
Finn, L. S., & Chernoff, D. F. 1993, PhRvD, 47, 2198
Flanagan, É. É., & Hughes, S. A. 1998, PhRvD, 57, 4535
Fontana, A., Salimbeni, S., Grazian, A., et al. 2006, A&A, 459, 745
Fregeau, J. M., Larson, S. L., Miller, M. C., O'Shaughnessy, R., & Rasio, F. A. 2006, ApJL, 646, L135
Fryer, C. L., Belczynski, K., Wiktorowicz, G., et al. 2012, ApJ, 749, 91
Gerosa, D., Kesden, M., Berti, E., O'Shaughnessy, R., & Sperhake, U. 2013, PhRvD, 87, 104028
Grindlay, J., Portegies Zwart, S., & McMillan, S. 2006, NatPh, 2, 116
Grishchuk, L. P., Lipunov, V. M., Postnov, K. A., Prokhorov, M. E., & Sathyaprakash, B. S. 2001, PhyU, 44, 1
Gültekin, K., Miller, M. C., & Hamilton, D. P. 2004, ApJ, 616, 221
Harry, G. M., for the LIGO Scientific Collaboration 2010, CQGra, 27, 084006
Heggie, D. C., & Giersz, M. 2014, MNRAS, 439, 2459
Hobbs, G., Lorimer, D. R., Lyne, A. G., & Kramer, M. 2005, MNRAS, 360, 974
Hogg, D. W. 1999, arXiv:astro-ph/9905116
Ivanova, N. 2015, Ecology of Blue Straggler Stars, ed. H. M. J. Boffin, G. Carraro & G. Beccari (Astrophysics and Space Science Library, Vol. 413; Berlin: Springer), 179
Ivanova, N., Heinke, C. O., Rasio, F. A., Belczynski, K., & Fregeau, J. M. 2008, MNRAS, 386, 553
Ivanova, N., & Taam, R. E. 2004, ApJ, 601, 1058
Kiminki, D. C., & Kobulnicky, H. A. 2012, ApJ, 751, 4
Kiminki, D. C., Kobulnicky, H. A., Ewing, I., et al. 2012, ApJ, 747, 41
Kreidberg, L., Bailyn, C. D., Farr, W. M., & Kalogera, V. 2012, ApJ, 757, 36
Kroupa, P. 2014, in Advances in Solid State Physics, Vol. 36, ed. D. Stamatellos, S. Goodwin & D. Ward-Thompson (Cham, Switzerland: Springer International Publishing), 335
Kulkarni, S. R., Hut, P., & McMillan, S. 1993, Natur, 364, 421
Lipunov, V. M., Postnov, K. A., & Prokhorov, M. E. 1997, MNRAS, 288, 245
Lyne, A. G., Burgay, M., Kramer, M., et al. 2004, Sci, 303, 1153
Mackey, A. D., Wilkinson, M. I., Davies, M. B., & Gilmore, G. F. 2008, MNRAS, 386, 65
Mandel, I., & O'Shaughnessy, R. 2010, CQGra, 27, 114007
Marassi, S., Schneider, R., Corvino, G., Ferrari, V., & Portegies Zwart, S. 2011, PhRvD, 84, 124037
Martini, P., Wagner, R. M., Tomaney, A., et al. 1999, AJ, 118, 1034
Mennekens, N., & Vanbeveren, D. 2014, A&A, 564, A134
Miller, M. C., & Lauburg, V. M. 2009, ApJ, 692, 917
Morscher, M., Pattabiraman, B., Rodriguez, C., Rasio, F. A., & Umbreit, S. 2013, ApJL, 763, L15
Nelemans, G., Yungelson, L. R., & Portegies Zwart, S. F. 2001, A&A, 375, 890
Nutzman, P., Kalogera, V., Finn, L. S., Hendrickson, C., & Belczynski, K. 2004, ApJ, 612, 364
O'Leary, R. M., Kocsis, B., & Loeb, A. 2009, MNRAS, 395, 2127
O'Leary, R. M., Rasio, F. A., Fregeau, J. M., Ivanova, N., & O'Shaughnessy, R. 2006, ApJ, 637, 937
O'Shaughnessy, R. 2013, PhRvD, 88, 084061
O'Shaughnessy, R., Belczynski, K., & Kalogera, V. 2008, ApJ, 675, 566
O'Shaughnessy, R., Kalogera, V., & Belczynski, K. 2005, ApJ, 620, 385
O'Shaughnessy, R., Kalogera, V., & Belczynski, K. 2010a, ApJ, 716, 615
O'Shaughnessy, R., Vaishnav, B., Healy, J., & Shoemaker, D. 2010b, PhRvD, 82, 104006
Özel, F., Psaltis, D., Narayan, R., & McClintock, J. E. 2010, ApJ, 725, 1918
Pan, Y., Buonanno, A., Boyle, M., et al. 2011, PhRvD, 84, 124052
Pan, Y., Buonanno, A., Buchman, L. T., et al. 2010, PhRvD, 81, 084041
Pannarale, F., Berti, E., Kyutoku, K., & Shibata, M. 2013, PhRvD, 88, 084011
Panter, B., Jimenez, R., Heavens, A. F., & Charlot, S. 2008, MNRAS, 391, 1117
Perets, H. B., & Kratter, K. M. 2012, ApJ, 760, 99
Pfahl, E., Podsiadlowski, P., & Rappaport, S. 2005, ApJ, 628, 343
Poisson, E., & Will, C. M. 1995, PhRvD, 52, 848
Portegies Zwart, S. F., & McMillan, S. L. W. 2000, ApJL, 528, L17
Postnov, K. A., & Yungelson, L. R. 2006, LRR, 9, 6
Repetto, S., & Nelemans, G. 2014, MNRAS, 444, 542
Rodriguez, C. L., Morscher, M., Pattabiraman, B., et al. 2015, PRL, submitted (arXiv:1505.00792)
Sadowski, A., Belczynski, K., Bulik, T., et al. 2008, ApJ, 676, 1162
Santamaría, L., Ohme, F., Ajith, P., et al. 2010, PhRvD, 82, 064016
Schutz, B. F. 2011, CQGra, 28, 125023
Shoemaker, D., & LIGO Scientific Collaboration 2010, Advanced LIGO Anticipated Sensitivity Curves, https://dcc.ligo.org/LIGO-T0900288/public
Sigurdsson, S., & Hernquist, L. 1993, Natur, 364, 423
Sippel, A. C., & Hurley, J. R. 2013, MNRAS, 430, L30
Somiya, K. 2012, CQGra, 29, 124007
Strolger, L.-G., Riess, A. G., Dahlen, T., et al. 2004, ApJ, 613, 200
Taylor, J. H., & Weisberg, J. M. 1989, ApJ, 345, 434
Thorne, K. S. 1974, ApJ, 191, 507
Tsang, D. 2013, ApJ, 777, 103
Tylenda, R., Hajduk, M., Kamiński, T., et al. 2011, A&A, 528, A114
Tylenda, R., Kamiński, T., Udalski, A., et al. 2013, A&A, 555, A16
Virgo Collaboration 2009, Advanced Virgo Baseline Design, Virgo Tech. Rep. VIR-0027A-09, https://tds.ego-gw.it/itf/tds/file.php?callFile=VIR-0027A-09.pdf
Voss, R., & Tauris, T. M. 2003a, MNRAS, 342, 1169
Voss, R., & Tauris, T. M. 2003b, MNRAS, 342, 1169
Webbink, R. F. 1984, ApJ, 277, 355
Wittkowski, M., Hauschildt, P. H., Arroyo-Torres, B., & Marcaide, J. M. 2012, A&A, 540, L12
Woods, T. E., & Ivanova, N. 2011, ApJL, 739, L48
Xu, X.-J., & Li, X.-D. 2010, ApJ, 716, 114
Yuan, T.-T., Kewley, L. J., & Richard, J. 2013, ApJ, 763, 9
Yusof, N., Hirschi, R., Meynet, G., et al. 2013, MNRAS, 433, 1114